Physics of the Earth and Planetary Interiors 356 (2024) 107259

Contents lists available at ScienceDirect

Physics of the Earth and Planetary Interiors

journal homepage: www.elsevier.com/locate/pepi

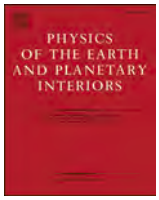

Tidal triggering of seismic swarm associated with hydrothermal circulation at Blanco ridge transform fault zone, Northeast Pacific

Sambit Sahoo [a], Batakrushna Senapati [a], Dibyashakti Panda [b], Shuanggen Jin [c,d], Bhaskar Kundu [a,*]

[a] Department of Earth & Atmospheric Sciences, NIT Rourkela, Rourkela 769008, India
[b] Department of Earth & Planetary Sciences, The University of New Mexico, Albuquerque, NM 87131, United States
[c] School of Surveying & Land Information Engineering, Henan Polytechnic University, Jiaozuo 454000, China
[d] Shanghai Astronomical Observatory, Chinese Academy of Sciences, Shanghai 200030, China

ARTICLE INFO

Keywords:
Ocean transform fault
Seismic swarm
Tidal periodicity
Resonance destabilization
Hydrothermal fluid

ABSTRACT

Seismicity associated with hydrothermal systems (e.g., submarine volcanoes, mid-oceanic ridges, oceanic transform faults, etc.) share a complex relationship with the tidal forcing and induced fluid flow process under different tectonic settings. The hydrothermal circulation drives the deformation at the brittle-ductile transition zone within a permeable brittle crust. Although the tidal loading amplitudes are too small to generate a brittle deformation, the incremental pressure exerted by the tidal loading can modulate the flow of hydrothermal fluid circulation and trigger the critically stressed faults or fracture zones. We present a compelling case of tidal modulation in seismicity along the Blanco Ridge Transform Fault Zone (BRTFZ), in the northeast Pacific. The strong diurnal and fortnightly periodicity has been observed in the deeper seismic swarm (7–15 km), whereas the shallow seismic swarm (0–7 km) does not exhibit any such tidal periodicity. The dominance of diurnal and fortnightly periodicity in the deeper seismic swarm is explained by the high amplitude tidal cycles providing additional stress on the fluid circulation at the crust-mantle boundary. Moreover, our robust statistical correlation of seismicity with tidal stress and resonance destabilization model under rate-and-state friction formalism suggests that the fault segments are conditionally unstable and more sensitive to periodic tidal stress perturbation.

1. Introduction

The gravitational attraction force from the Sun and moon during rotational cycles in particular orbits create deformations leading to periodic fluctuations on Earth's surface. Following the law of gravitational attraction, the mass of the Moon is much less (~27 million times) than that of the Sun, however the moon generates a stronger lunar tidal effect due to the much greater distance of the Sun (~400 times) from the Earth (Lowrie, 2011). The unequal attractions from the celestial bodies produce tidal-loading deformations at respective periodic tidal constituents, exerting displacement, acceleration, tilt, and strain effects on the Earth's surface (Agnew, 1997). Moreover, the amplitude of the lunar constituents is always greater than the solar and lunisolar counterparts. Predominantly, there are 37 major tidal constituents with 32 short-period (J1, K1, K2, L2, LAM2, M1, M2, M3, M4, M8, MK3, 2MK3, MN4, MS4, MU2, N2, 2 N2, NU2, O1, OO1, P1, Q1, 2Q1, R2, RHO, S1, S2, S4, S6, 2SM2, T2) and 5 long-period constituents (SSA, SA, MM, MF and MSF) (Matsumoto et al., 2001). These lunisolar gravitational forces produce periodical tidal loading at various stress intensities and periods on the critically stressed fault systems. The varying periods of tidal loading, also known as the tidal constituents, are the greatest during the diurnal and semi-diurnal cycles (Agnew, 1997, 2012). It has been observed that the amplitude of the tidal cycles varies at different geographical regions around the globe, which has been extensively explored using satellite altimeter data from Topex/Poseidon (Ray, 1999). The periodic stress perturbations due to tidal cycles reveal that, under certain conditions, the amplitude of stress can be significantly lower or higher during alternate low and high amplitude tidal cycles. This can be observed at alternate low and high amplitude semidiurnal cycles, appearing at a diurnal period (Wilcock, 2009). Therefore, it is crucial to probe the ability of this periodic higher tidal forcing to modulate, induce or trigger earthquakes in a diverse type of tectonic setting. This can be also helpful

* Corresponding author at: Department of Earth & Atmospheric Sciences, NIT Rourkela, Rourkela 769008, India.
E-mail address: rilbhaskar@gmail.com (B. Kundu).

https://doi.org/10.1016/j.pepi.2024.107259
Received 25 August 2023; Received in revised form 15 May 2024; Accepted 11 September 2024
Available online 12 September 2024

in providing important information related to the condition of state-of-stress on the seismogenic fault system deep underneath the oceanic basin.

The tidal loading and modulations related to triggering were recognized more than a century ago, despite the equivocal relationship between earthquakes and the specific triggering mechanism (Schuster, 1897). However, seismicity at multiple regions associated with diverse tectonic settings has been reported with tidal triggering. The regions are commonly marine or coastal in nature where the ocean tidal loadings are higher such as coastal subduction zones (Cochran et al., 2004; Tanaka et al., 2006; Thomas et al., 2009; van der Elst et al., 2016), and deep sea mid-ocean ridges (Sahoo et al., 2021; Wilcock, 2001, 2009; Tolstoy et al., 2002; Wilcock et al., 2016; Bhatnagar et al., 2016; Tan et al., 2018; Scholz et al., 2019). The modulations are also commonly reported in volcanic and hydrothermal systems where the fluid pressure is maximum (McNutt and Beavan, 1984; Petrosino et al., 2018; Sahoo et al., 2022; Petrosino and Dumont, 2022). The extraterrestrial examples of tidal modulations can also be found in deep and shallow moonquakes (Goulty, 1979; Lammlein, 1977; Lognonné, 2005; Minshull and Goulty, 1988; Senapati et al., 2024). Although in many cases signatures are reported to be absent for tidal modulations of seismicity of large samples (Heaton, 1975; Vidale et al., 1998). Enhancement of significant tidal triggering signatures from shallow focus and low magnitude seismic events was reported by Métivier et al. (2009), analyzing a global seismic event dataset of ~442,412 low magnitude and shallow events. Established on the laboratory experiments and the rate-and-state friction modeling (Lockner and Beeler, 1999; Perfettini and Schmittbuhl, 2001), the correlation between tides and seismicity events (mostly microseismic in nature) are significant if the seismic event has a nucleation event is similar to the tidal loading perturbation period (Beeler and Lockner, 2003; De Lauro et al., 2013; Ader et al., 2014; Heimisson and Avouac, 2020). It is noted that transient stress perturbations in porous materials, can change the mobility of fluids and associated permeability (Manga et al., 2012). Under critically stressed conditions of a fault system, the fault frictional parameters are case sensitive and slight variations can produce scatterings. Also, the phase lags between the period of external stress perturbation and the periodic response of the fault system may produce absence of correlations in the resonance signatures (Perfettini and Schmittbuhl, 2001). This disturbs the tidal modulation signatures of the particular seismicity dataset.

Following these observations, we can infer the complexity of the nonlinear correlation between the earthquake modulations and the tidal loading amplitude on the fault system (Rydelek et al., 1992; Lockner and Beeler, 1999; Beeler and Lockner, 2003). Hence more scientific attention is needed for understanding the mechanism of tidal triggering and associated seismicity modulation. Further, prominent periodicities of

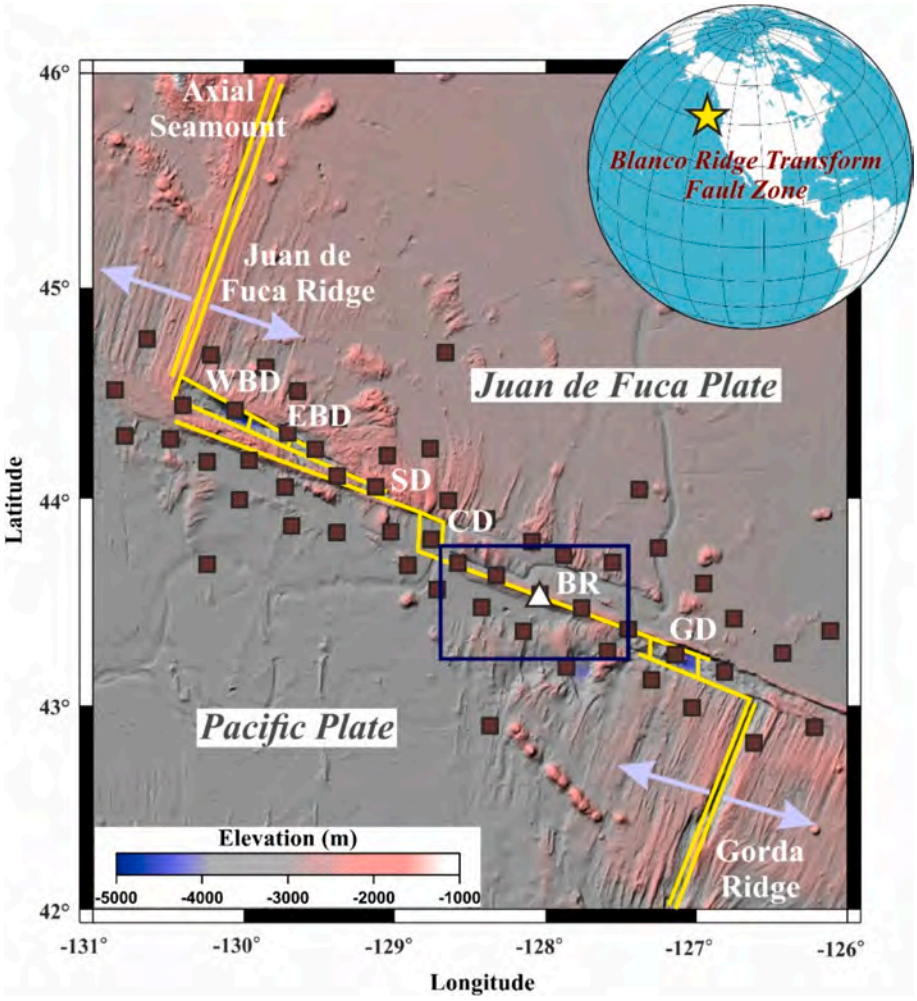

Fig. 1. Tectonics and bathymetry map of the Blanco transform fault system. The Blanco Ridge (BR) region has been marked by a blue rectangle (enlarged panel in Fig. 2a). The location of the ocean-bottom seismometers (OBS) stations is marked by squares. The white triangle along the transform fault marks the location (43.5°N, −128°E) over which tidal stress has been calculated.The bathymetric depressions from west to east are West Blanco (WBD), East Blanco (EBD), Surveyor (SD), Cascadia (CD) and Gorda (GD). The bathymetry base map is generated using the data archived from the General Bathymetric Chart of the oceans (https://download.gebco.net/). (For interpretation of the references to colour in this figure legend, the reader is referred to the web version of this article.)

diurnal (24 h) and weekly basis (7 days), have been reported from the seismicity observed in continental tectonic settings. It is often observed due to ambient cultural disturbance from man-made ground traffic, operating machinery, and building shaking as apparent artificial/anthropogenic periodicities (Atef et al., 2009; Díaz et al., 2017), which leads to difficulties in discriminating the natural periodicities. However, the seismicity associated with the submarine volcanoes, mid-oceanic ridges, or oceanic transform fault systems in the oceanic counterparts can be regarded as the ideal one to investigate the mechanism of tidal triggering more efficiently, as the regions are usually devoid of ambient cultural noise. Further presence of magmatic (or hydrothermal) fluid circulation makes this region more sensitive to tidal-induced stress perturbation (Lockner and Beeler, 1999).

Based on this motivation, we have investigated the seismicity associated with the Blanco Ridge Transform Fault Zone (BRTFZ), a prominent linear segment that exhibits relatively higher seismic coupling in the northeast Pacific, where hydrothermal circulation in the upper mantle/lower crust plays a critical role which is again highly suitable for tidal triggering and modulations (Braunmiller and Nábělek, 2008; Kuna et al., 2019) (Fig. 1). Although, tidal triggering and seismicity modulation have been extensively reported around the western coast of North America (Wilcock, 2001; Tolstoy et al., 2002; Wilcock et al., 2016; Bhatnagar et al., 2016; Tan et al., 2018; Scholz et al., 2019; Sahoo et al., 2021), tidal modulations process at BRTFZ has not been explored yet. Moreover, the seismicity at the in-general normal faults in the region of the north-west Pacific is prone to compressive forces during the low tides (Wilcock, 2009).

In the study region of BRTFZ, we have investigated the existence of tidal triggering and associated mechanisms as well as the exact frictional condition and sensitivity of the tidal triggering potential of the seismic swarms. In order to explore, we have analyzed the seismicity modulation by tidal triggering and a resonance phenomenon explaining the modulation process with the concept of fault destabilization, considering rate-and-state friction-governed fault interfaces. In this article, we have presented the tectonic framework of the Blanco Ridge Transform Fault Zone (BRTFZ), and the precisely located seismicity by ocean-bottom seismometers (OBS) experiments along the full length of BRTFZ, the tidal model and resonance destabilization models are described in the materials and methods. In the results section, we have used systematic statistical analysis, and tidal correlation and tried to model the rate-and-state frictional conditions by the resonance destabilization process to present our key findings. We have also discussed the possible explanations for the observed signatures of tidal loading-induced seismicity modulation and the importance of hydrothermal fluid circulations at the crust-mantle transition zone of the BRTFZ, comparing them with the reported global tidal correlations before arriving at a conclusion.

2. Tectonic framework of Blanco ridge transform fault zone (BRTFZ)

The Blanco Transform Fault in the western Pacific coast is a right lateral transform fault zone of about 350 km long, lying between Juan de Fuca and the Pacific plate. It runs northwest off the coast of Oregon in the northeast Pacific plate, extending from the Gorda Ridge in the south to the Juan de Fuca Ridge in the north (Fig. 1). This seismo-tectonically active oceanic transform fault zone is divided into a number of morphologically and seismologically distinct segments (Embley and Wilson, 1992; Braunmiller and Nábělek, 2008; Kuna et al., 2019). However, the Blanco Ridge Transform Fault Zone (BRTFZ) represents a ~ 130 km long, northwest-southeast trending prominent linear segment of Blanco Transform Fault, that exhibits a significantly higher coupling for seismicity (Braunmiller and Nábělek, 2008). It has been reported that along the BRTFZ, two prominent asperities break quasi-periodically with earthquake moment magnitude $6.0 < M < 6.5$ (Braunmiller and Nábělek, 2008). A prominent 10 km long bathymetrically and geometrically anomaly zone demarcates especially those two asperities along BRTFZ (Kuna et al., 2019) (Fig. 1). The association of seismicity along BRTFZ represents a significant spatial concentration between 3 and 7 km depth range in the oceanic crust and in the mantle depth between 8 and 13 km, leaving a quiet aseismic zone prominently at 7–8 km depth range, which is below the Moho and along the strike-wise vertical fault cutting across the lithosphere (Fig. 2). Further, the thermal modeling approach predicts the depth limit of seismicity along the BRTFZ (i.e., by the 600 °C isotherms in Fig. 2) (Kuna et al., 2019). Hydrothermal circulation is attributed to the brittle-ductile transition zone present at depths marginally shallower from 600 °C isotherms. The serpentinized mantle that is present above 600 °C isotherms provides the pathway for hydrothermal circulation with the presence of permeable and fractured rheology (Kuna et al., 2019).

3. Material and methods

3.1. Seismicity catalog

From September 2012 to October 2013 an ocean-bottom seismic (OBS) experiment was done by deploying Güralp CMG3T seismometers with 30 broadband and L-28LB seismometers with Mark Product of 25 short-period ones. These were also co-located with differential pressure sensors of Scripps Institution of Oceanography along the full length of the Blanco Transform Fault (Kuna et al., 2019) (Fig. 1). This experiment has located more than 1650 earthquake events with local magnitude (M_L) of 0.8–5.5 at the BRTFZ. From the recorded catalog during that experiment, elimination of events has been processed for the events with first arrivals missing at 1 of the 3 closest stations, fewer than six arrivals at the 13 closest stations, and azimuthal gap between stations at larger than 110°. Therefore, here we have considered only the best-recorded seismicity catalog containing 1626 events for subsequent investigation of tidal triggering (Kuna et al., 2019).

3.2. Magnitude completeness, b-value estimation, declustering and clustering approach

In order to find out the threshold of completeness (Mc), we have also analyzed the entire catalog during the study period with Gutenberg-Richter (GR) law by maximum curvature method. To analyze the seismicity catalog, the clustered events (only seismic swarms excluding aftershocks) and declustered events (only master events excluding swarms and aftershocks) were found out using the nearest neighbourhood method by Zaliapin and Ben-Zion (2013) and declustering method by Reasenberg (1985). Both depth-wise clustered and declustered catalogs were analyzed with GR law for Mc estimation and b-value estimation using the maximum likelihood approach (Aki, 1965). We have also distributed the catalog for depth wise variations as above and below the aseismic zone at around 7 km.

3.3. Periodicity analysis using power spectrum

To establish the tidal periodicity in the seismicity catalog during the OBS experiment, we have implemented a power spectrum analysis, by adapting the dataset format in the hourly event numbers, for the entire period of the seismicity time series. The Power spectrum $S_{xx}(w)$of a time series $x(t)$ described the distribution of power into frequency components composing that signal and expressed as:

$$\left.\begin{aligned} P &= \lim_{T\to\infty}\frac{1}{T}\int_0^T |x(t)|^2 dt \\ S_{xx}(w) &= \lim_{T\to\infty} E\left[\left|\hat{x}(w)\right|^2\right] \end{aligned}\right\} \quad (1)$$

where P = average power, x(t) = time series, S_{xx} = power spectrum and E = energy of a signal.

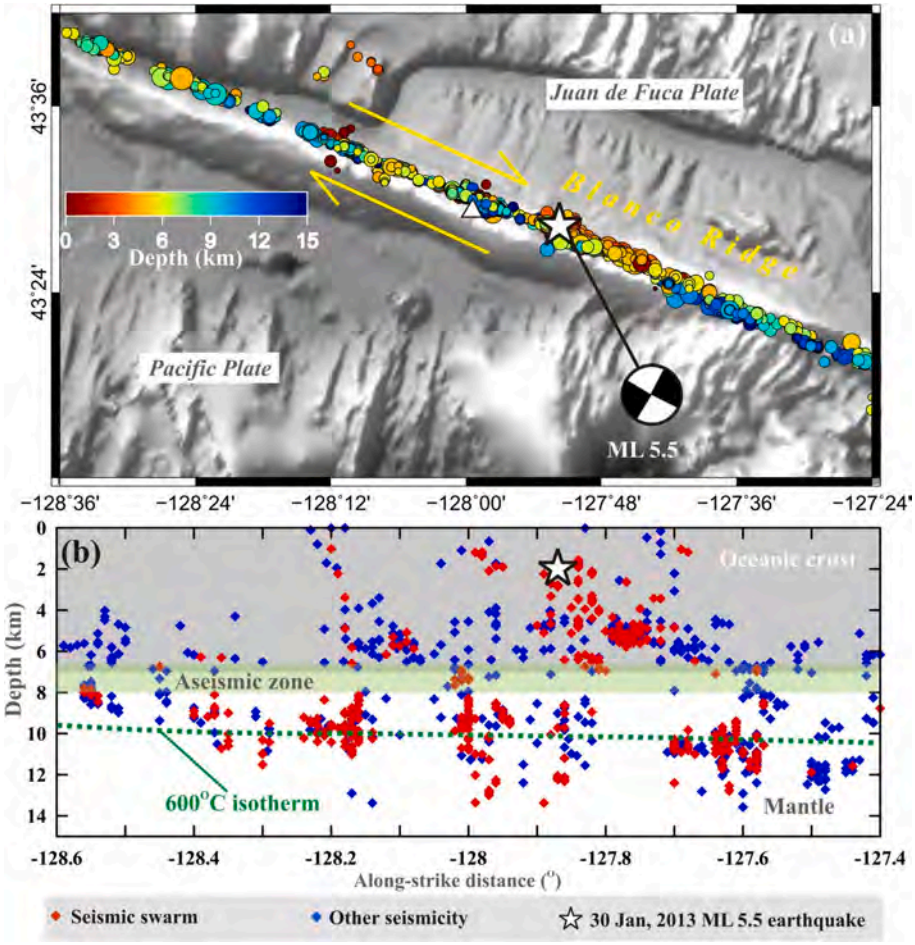

Fig. 2. (a) Bathymetric map of the Blanco Ridge Transform Fault Zone (BRTFZ) with the spatial distribution of earthquake epicenters (Mc 2.0, spanning from September 2012 to September 2013). The white triangle along the transform fault marks the location (43.5°N, −128°E) over which tidal stress has been calculated. The white star marks the January 30, 2013, M_L5.5 earthquake, so far the largest event captured by the OBS experiment. (b) Depth wise distribution of seismicity (i.e., along-strike cross-sectional view). Note spatially, mantle earthquakes occur in small clusters or swarms. The dashed green line indicates the 600 °C isotherm estimated by the thermal models based on the tectonic slip rate of 56 mm/yr. (For interpretation of the references to colour in this figure legend, the reader is referred to the web version of this article.)

3.4. Tidal model

For quantification of tidal loading from the ocean loading as well as solid earth loading, we have estimated longitudinal strains with directions of north-south 0° and east-west 90°, along with shear strains acting on the directions of north-east, and the volumetric strain acting on the vertical direction on the major fault azimuth. The strains were estimated for both ocean tides and combined ocean tides along with body tides by calculating the estimated total tides and ocean tides using the widely accepted SPOTL program (Some Programs for Ocean Tidal Loading) (Agnew, 1996, 1997, 2012). This program is widely accepted for the calculation of tidal loading stress which adopts a model of spherical and elastic Earth with second-degree Love numbers (i.e. h = 0.6114, k = 0.3040, and l = 0.0832) by means of Green's functions taken from the earth model as Gutenberg-Bullen (Farrell, 1972), including the Cartwright-Tayler constituent amplitudes. The model significantly computes the tidal strains and appropriate time-series straight from the expected sites of the Sun and the Moon (Agnew, 1997). For this calculation, the strains (extension positive) were estimated by using the model for global oceans (GOT4.7) for tides combined with the tidal model for the regional ocean by Oregon State University (OSU) used for the United States Western coast (Egbert and Erofeeva, 2002). Calculated estimations included the effects of major tidal constituents (K1, K2, M2, N2, O1, P1, Q1, and S2) which are short-period (<24 h) in nature. For the estimation of strain to stress conversion, we have adopted a standard Poisson ratio of 0.25 and an effective Elastic modulus of 30 GPa (Sahoo et al., 2021). During the conversion of strains to stress, linear elastic constitutive equations were adopted. Using strain rotation, the tidal Fault normal stress (FNS) and Right lateral shear stress (RLSS) has been resolved on the steeply dipping transform fault plane (strike: 292°, dip: 85°, rake: +180°) at a central point over the BRTFZ (43.5°N, −128°E) (Figs. 1, 2). Further, the Coulomb failure stress (CFS) was estimated by considering a friction coefficient (μ) of 0.3 with the effects from both the shear and normal stress. We have computed tidal stress contribution for both total tidal (ocean+solid earth) and ocean tidal loading effects. For the quantification of the respective seismicity and tidal stress correlation amount, we have undertaken the the excess event percentage (N_{ex}) approach (Sahoo et al., 2021; Thomas et al., 2012). We have explained our analysis further in Section 4.3.

3.5. Tidal stress-induced resonance destabilization model

The resonance destabilization model has been well-studied theoretically (Perfettini et al., 2001; Perfettini and Schmittbuhl, 2001), using natural observations (Lowry, 2006; Panda et al., 2018; Senapati et al., 2023a) and analyzing through the laboratory-based experiment and observations (Boettcher, 2004). It has been proposed that the fault system may change from a stable domain to a stick-slip domain due to

the slight variation in the amplitude of periodic external stress. Although periodic tidal load-induced stress perturbation is varying at a smaller range of Pa to kPa, the amount of stress is sufficient to modulate the seismic swarms under the conditions of rate-and-state friction by destabilizing the fault system. The oscillatory (or harmonic) amplitude of fault parallel shear stress τ_1 and fault normal stress σ_1 with stress perturbation of period T, generating the response velocity V (Perfettini, 2000; Senapati et al., 2022; Senapati et al., 2023a), is expressed by:

$$V = V_L + Im[V_1 exp(i\omega t)] \tag{2}$$

where $V_1 = \rho\nu\, exp(-i\gamma\nu)$, V_L is the long-term velocity (or plate velocity), the imaginary part is represented by *Im*, and $\omega = \frac{2\pi}{T}$. The parameters $\rho\nu$ and $\gamma\nu$ are given by:

$$\left.\begin{aligned} \rho\nu &= \frac{V_L q \tau_{ss}}{k d_c}\sqrt{\frac{\left\{q\left(\epsilon_\sigma\left(1-\frac{\alpha}{\mu_{ss}}\right)-\epsilon_\tau\right)\right\}^2+(\epsilon_\sigma-\epsilon_\tau)^2}{\left(1-\frac{k_c\left(\frac{q}{q_c}\right)^2}{k}\right)^2+\left(q\left(1-\frac{k_c}{k}\right)\right)^2}} \\ tan(\gamma\nu) &= \frac{q^2\left(1-\frac{k_c}{k}\right)\left[\left(\epsilon_\sigma\left(1-\frac{\alpha}{\mu_{ss}}\right)-\epsilon_\tau\right)\right]-(\epsilon_\sigma-\epsilon_\tau)\left(1-\frac{k_c\left(\frac{q}{q_c}\right)^2}{k}\right)}{q\left[\left(\epsilon_\sigma\left(1-\frac{\alpha}{\mu_{ss}}\right)-\epsilon_\tau\right)\right]\left(1-\frac{\left(\frac{q}{q_c}\right)^2}{\frac{k}{k_c}}\right)-q\left(1-\frac{1}{\frac{k}{k_c}}\right)(\epsilon_\sigma-\epsilon_\tau)} \end{aligned}\right\} \tag{3}$$

where $q = \frac{V_L}{d_c}\frac{2\pi}{T}$ is the non-dimensional frequency, effective normal stress is termed as σ_*, $\epsilon_\sigma = \frac{\sigma_1}{\sigma_*}$ is the applied FNS to the effective FNS ratio, $\epsilon_\tau = \frac{\tau_1}{\mu_{ss}\sigma_*}$ is the applied external RLSS to the steady-state RLSS ratio, the critical slip distance is termed as d_c, parameters of rate-and-state friction are termed as a and b, $\mu_{ss} = \mu_* + (a-b)log\left(\frac{V_L}{V_*}\right)$ is the frictional coefficient in the steady-state, $k_c = \frac{(b-a)\sigma_*}{d_c}$ is the critical stiffness, whereas the slipping segment stiffness is k, and the constant is α (Dieterich, 1987; Perfettini et al., 2001), $q_c = \sqrt{\frac{b-a}{a}}$ is critical non-dimensional frequency. $T_c = 2\pi\sqrt{\frac{a}{b-a}}\frac{d_c}{V_L}$ is termed as the critical periodic constituent of the contributing external stress variation, and therefore T is the external stress perturbation period. In order to address further tidal load induced seismicity modulation process associated with the BRTFZ at different tidal constituents, we have adopted and used the rate-and-state friction formalism with this resonance destabilization model (Senapati et al., 2023a).

4. Results

4.1. Analysis of the seismic catalog

The Blanco ridge transform fault Zone (BRTFZ) associated seismicity is characterized by the clustered nature of seismic swarms, mainshock-aftershock sequences, and other un-clustered earthquakes distributed from crust to mantle along the fault plane, cutting across the lithosphere (Fig. 2). Further, the BRTFZ ruptured on January 30, 2013, of M_L5.5 strike-slip earthquake, so far the most significant event during ocean-bottom seismometers (OBS) experiment. Moreover, this strongest event reportedly gave rise to a sequence of aftershocks containing around 37 events, focused in the barrier area (Kuna et al., 2019). Therefore, to establish tidal load-induced seismicity modulation along BRTFZ and to represent depth-dependent characterization of tidal modulation for clustered seismic swarms and other un-clustered master events, we have implemented the nearby neighbourhood clustering approach (Zaliapin and Ben-Zion, 2013) and declustering method by Reasenberg (1985) respectively. The clustering analysis has revealed that the clustered events with a unimodal distribution show the characteristics of swarm events due to the linear linking of the spanning trees (Fig. 3). Hence the clustered events are separated as the seismic swarms and the declustered events are separated as the master or single events according to the nearest neighbourhood distance (Fig. 3a). The distribution of the clustered and unclustered events in particular time-space can be observed through the presence of the event pairs in the rescaled time and distance (Fig. 3b) and the linear linking of the clustered black circles and red circles with the help of dashed lines (Fig. 3c). Here the blue circles are the unclustered events and black circles are the last generation of the clustered events. The darkness of the red circles gives an idea about the higher number of events in each circle. Fig. 3d shows the aftershock distribution for each magnitude bin. The white circles correspond to the main event magnitude and number of aftershocks for the event. The distribution shows that the number of aftershocks for the large magnitude event (M5.5) is greater than for the smaller magnitude events, which also follow the general linear trend between the main event and aftershocks. The gray error bars associated with the white circles correspond to the standard deviations for each point. The distribution falling within either part of the slope (fitted curve of linear trend as red line) suggests the confidence levels of the slope. Therefore, the aftershock events were removed from the seismic swarms (clustered events) and the master (declustered) events, which have been analyzed for possible tidal modulations in the subsequent section.

To find out the threshold of completeness (Mc), we have also analyzed the entire catalog during the study period with Gutenberg-Richter (GR) law in the maximum slope curvature method of seismicity distribution. The method was performed in addition with the b-value approximation for the depth-wise swarms (and master event) catalog, by maximum likelihood approach (Aki, 1965). From the analysis of GR-law for Mc and b-value estimation, it has been observed that the b-value for the total catalog is 0.95 ± 0.06 with Mc = 2, which is consistent with the regional global average b-values for seismic swarms at hydrothermal systems (Gutenberg and Richter, 1944). However, depth-wise systematic analysis of clustered seismic swarms and master events show inconsistency in b-values estimation (Fig. 4). The uncertainties related to Mc and b-value estimations were calculated by the slope fitting of the curves to the natural observation of the seismicity distribution and universal values for the maximum likelihood of the b-value (Aki, 1965; Kundu et al., 2012) Clustered seismic swarms have a relatively higher b-value (1.12 ± 0.11 with Mc = 2), in contrast to the master events (0.78 ± 0.06 with Mc = 2). Even, deeper seismic swarms at 7–15 km depth show much higher b-values (1.29 ± 0.15 with Mc = 2) (Fig. 4). However, the magnitude completeness is almost constant for all the differentiated catalogs for the study period (i.e., Mc = 2) for all the cases of analysis (Fig. 4).

4.2. Characterization of seismic periodicity

To find out the presence of tidal periodicity signal for the events, the seismic swarms and master events, at shallow (0–7 km) and deeper depth (7–15 km) regime were analyzed considering the catalog completeness. This systematic analysis shows a significant difference in tidal periodicity in the seismic swarms at the shallow region and deeper region (Fig. 5). It has been observed that the seismic swarms that occurred in the mantle at deeper depth (7–15 km), exhibit a significantly strong diurnal periodicity of K1 tidal constituent (~365 yr^{-1}, 23.93 h, larger lunar elliptical diurnal constituent) and a fortnightly periodicity (~28 yr^{-1}, MF = 13.66 days, lunisolar fortnightly constituent) (Fig. 5). However, tidal periodicity is completely lacking for the swarm occurred at shallow depth 0–7 km (Fig. 5).

Although the dominant semi-diurnal tidal periodicity as M2 tidal

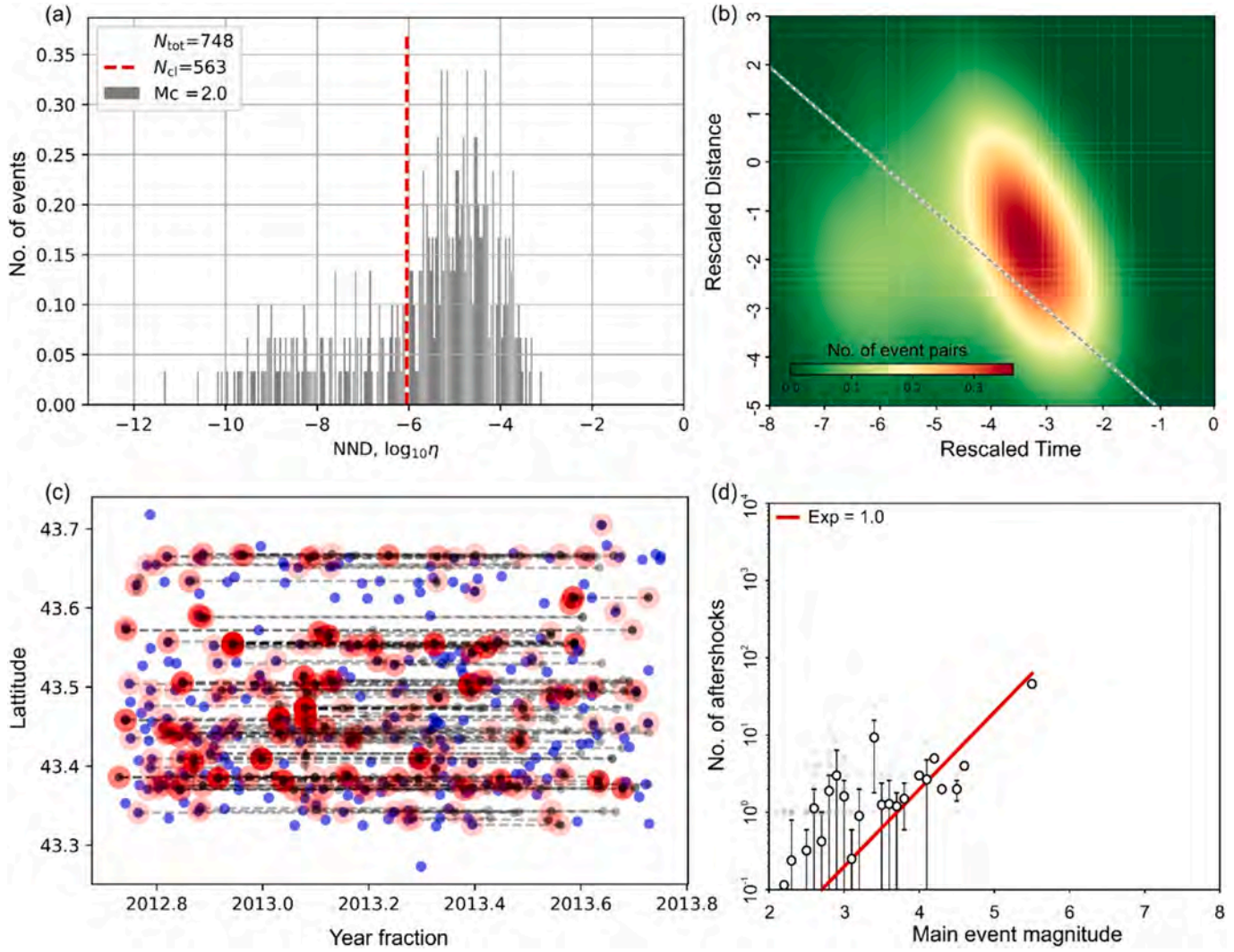

Fig. 3. Clustering analysis of the seismic events showing the distribution of the events with the number of total, clustered and master events separated by the red dotted line in the nearest neighbourhood distance (NND) vs No. of evnts graph (a). The nearest neighbor in the distance vs. time graphs shows the distribution of the clustered events (b). The spanning tree of the clusters shows that the nature of the clusters is mostly swarm-like due to the chain appearance of the linked clusters (c). Distribution of a number of aftershocks for magnitude-wise main events along with the standard deviations (white circles and gray lines) shows the average trend of the number of aftershocks for the main events (clustered events or swarms and declustered or master events) in the red fit curve (d). (For interpretation of the references to colour in this figure legend, the reader is referred to the web version of this article.)

constituent is not prominent in the seismicity catalog, the presence of strong diurnal K1, and Fortnightly MF periodicity in the deeper seismic swarms cannot be considered an artifact. Unlike the continental tectonic settings, the seismicity associated with the submarine hydrothermal regions is devoid of anthropogenic cultural noise. We have also analyzed the magnitude completeness of the catalog with depth and time change and found that it was overall consistent. Hence, the diurnal (K1) periodicity exhibited in the deeper seismic swarms can be considered natural. To confirm the tidal modulation in the deeper depth seismicity, we have further analyzed the correlation between the tidal loading and seismicity occurrence.

4.3. The seismicity and tidal load correlation

To check the robustness of the tidal triggering from tidal load phenomena, we have computed tidal stresses exerted by the tidal loading at a general point over the BRTFZ (43.5°N, −128°E) and correspondingly, tidal stresses have been resolved on the fault planes, considering contribution from both ocean tide and solid-earth tide (Fig. 6a). The resolved stress on the fault plane has been presented as Fault Normal Stress (FNS), Right Lateral Shear Stress (RLSS), and Coulomb Failure Stress (CFS) in the representative tidal time series (Fig. 6a), considering contribution from both total tide (ocean+solid earth) and ocean tide. Further, the corresponding phase of seismicity are estimated by defining phase angles with two peaks representing 0° and 360° and alternate peak and trough cycles between 0° to 360° of tidal stress perturbations (Fig. 6b). For the quantification of the respective seismicity and tidal stress correlation amount, we have computed the excess event percentage (N_{ex}). Adopting approaches from Thomas et al. (2012) and Sahoo et al. (2021), N_{ex} numbers can be defined as:

$$\textit{Percentage of excess event}\ (N_{ex}) = \frac{N_{actual} - N_{expected}}{N_{expected}} \times 100 \quad (4)$$

where $N_{expected}$ and N_{actual} are the expected and actually occurring events under a positive tidal stress domain respectively. Here earthquake occurrence times are under assumptions of random distribution where the events are expected to be occurring under positive tidal stress domain. The expected events are calculated on the basis of the ratio of positive stress domain available from the total time series and the distribution of the expected event according to the ratio of the positive

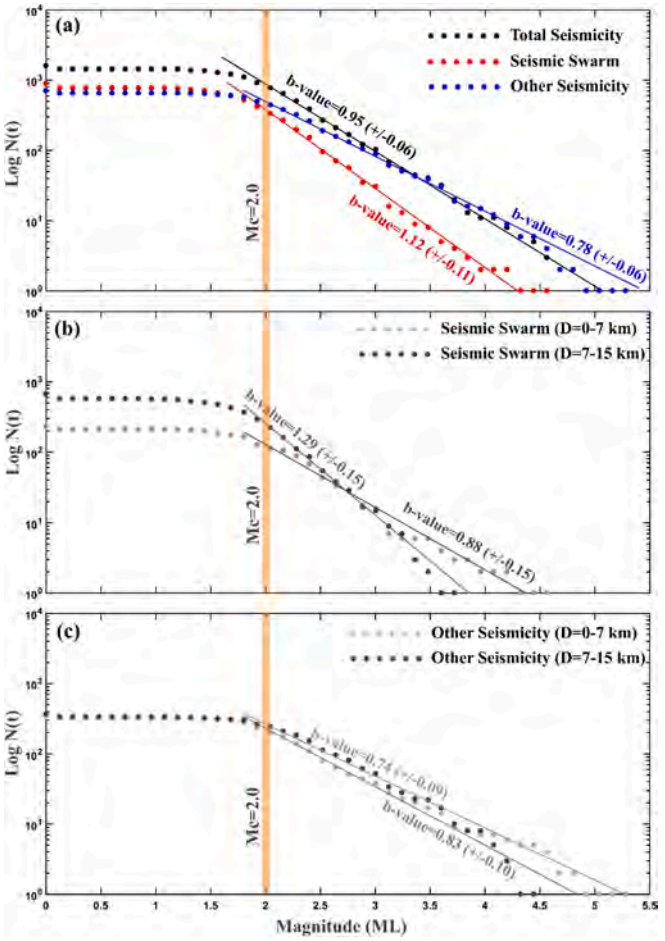

Fig. 4. (a) Magnitude of completeness (Mc) of the total seismicity catalog, seismic swarm and other seismicity events spanning from September 2012 to September 2013. (b, c) Magnitude of completeness estimation by considering depth wise distribution of the seismic swarm and other seismicity events (i.e., shallow: 0–7 km and deeper: 7–15 km). Note the high b-value of the swarm seismicity, which possibly suggests presence of magmatic (or hydrothermal) fluid circulation. Overall the Mc value remains the same (i.e., 2.0) for all seismicity catalogs.

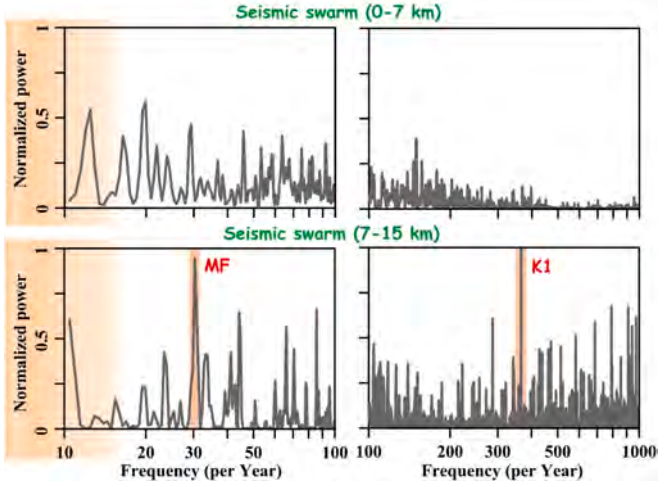

Fig. 5. Power spectra analysis for seismic swarm catalogs considering different depth intervals. Note significant diurnal (K1) and fortnightly (MF) tidal periodicities in the seismic swarm catalog. However, shallow seismic swarms (0–7 km) no significant tidal periodicities are observed.

domain. The difference between actual and expected number of events is either the excess or depleted number of events and thus can be positive or negative. Hence, higher values suggest a greater correlation of the events to the respective stress domain. Also, positive values suggest the presence of an excess number of events under the positive domain, and negative values show a depleted number of events under the positive domain. The negative values also imply an excess number of events in the negative domain as the total number of events is constant (Sahoo et al., 2021, 2024; Thomas et al., 2012). After that, we have presented a polar bar chart for the respective depth-wise catalogs of seismic swarm. For the smooth presentation, we have adopted 10° bins where the phases are grouped, and each bin is consequently normalized by $N_{expected}$ under the respective tidal stress range of the bins (Fig. 6c-d-e). The ratio of the N_{actual} and $N_{expected}$ is represented by the specific radius present in the polar bar chart, which can be also defined as $N_{ex} + 1$ of respective range of bins (Fig. 6c-d-e). Strong cases of tidal triggering are suggested with more than 100 % $N_{ex} + 1$ radius values in each chart and vice versa.

It has been suggested that stress from tidal loadings is predominantly volumetric. Hence, fault azimuth selection has negligible effect on N_{ex} value for the FNS, while considerably effective on the RLSS (Thomas et al., 2009). However, with predominantly linear segments and uniform fault azimuth, associated with the Blanco Ridge Ocean transform fault zone (BRTFZ), we can avoid such complexity in the present case. From this robust statistical analysis to correlate tidal stress and seismicity (Fig. 6), the radius of the phase plots for deeper seismic swarms are almost entirely observed to be more than 100 % of expected value contours (Fig. 6d-e) in comparison to clustered shallow seismicity. This represents the extreme sensitivity of deeper seismic swarms to tidal stress. Further, the deeper seismic swarms appear to be induced by FNS with more events at a negative stress domain or negative N_{ex} value. Whereas, the same swarms represent excess events at the positive stress domain or positive N_{ex} value with the RLSS. The presence of excess events during negative stress domain of FNS indicates that the seismogenic events predominantly occur during negative FNS or peak low tides (i.e. compressional normal stress) whereas, RLSS sensitivity on deeper seismic swarms the represents the signatures of high fluid pressure (Lockner and Beeler, 1999; Cochran et al., 2004). Further, the CFS observed with a higher percentage of encouraging or positive values of the N_{ex} imparts effective unclamping on the fault plane system. Similarly, we have also presented N_{ex} number percentages of respective catalog and polar bar charts representing each shallow level of seismic swarms (Fig. 6d-e), however, we have observed either weak or insignificant correlation of tidal stress modulation in a comparison with the deeper seismic swarms (Fig. 6d-e). Moreover, the time-series correlation of Fault normal stress (ocean tidal loading) and deeper seismic swarms (7–15 km) also exhibit the abundance of events at higher amplitude low tidal cycles (Fig. 7). The histogram of events under particular tidal stress suggests a higher distribution of events during the higher compressional stress (Negative normal stress) (Fig. 7). This also indicates the amplitude sensitive effectiveness of tidal stress on the seismic swarms.

4.4. Tidal stress induced resonance destabilization and seismicity modulation

To probe the exact frictional condition and sensitivity of the tidal triggering potential of the seismic swarm, we have developed a tidal induced resonance destabilization model (modeling approach described in corresponding section). In other words, we have investigated the chances of amplification for resonance process under rate-and-state friction and supporting model parameters for possible seismicity modulation along the BRTFZ (Fig. 8). For the resonance related destabilization getting induced by the tidal stress perturbations, some criterias should be fulfilled. i.e. The fault portion length (R), should be near to fault portion critical length (R_c), excitation period or perturbation period (T) should be near to period of critical excitation (T_c), and the cost function (C) should be nearly equal or very close to zero. For the

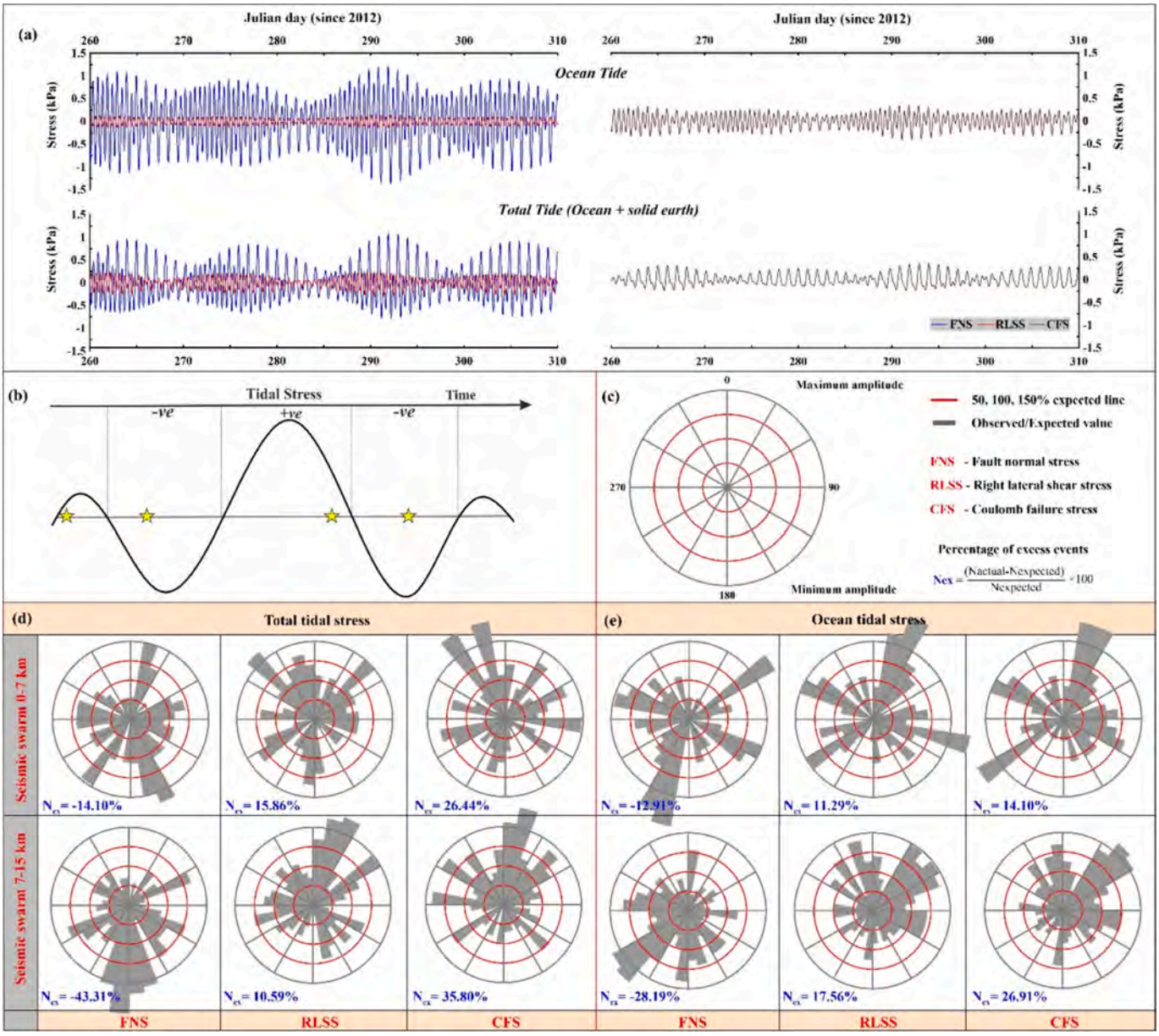

Fig. 6. (a) Representative tidal stress (FNS: Fault Normal Stress and RLSS: Right Lateral Shear Stress; CFS: Coulomb failure stress) of Julian days of 2012 for both Total tide (Ocean+Solid Earth) and Ocean tide. (b) Schematic diagram showing the variation of Total tidal stress and the phase of seismic events associated with it. The peak and trough of the time series are assigned phase values of 0° and 180° respectively. Dashed lines indicate the region of positive and negative tidal stress domains. Yellow stars represent hypothetical earthquakes, which correspond to either positive/negative stress fields. (c) Gray shaded areas indicate the ratio of observed to the expected number of events in each 10 degree phase bin. Thin red lines are 50 %, 100 % and 150 % expected value contours. Polar phase plots and percent of the excess (N_{ex}) values of both seismic swarms and other events (Mc 2.0, spanning from September 2012 to September 2013) with varying depth by considering FNS, RLSS, and CFS components of Total tidal stress(d) and Ocean tidal stress(e). Note that in case of seismic swarms, the N_{ex} of CFS shows higher positive values, indicating a possibly increase of pore fluid pressure which facilitates tidal triggering of seismic swarms. (For interpretation of the references to colour in this figure legend, the reader is referred to the web version of this article.)

respective analysis, the specific periods of perturbation as the periods of resonance modulation are taken as fortnightly and diurnal (i.e. T as MF = 13.66 days, K1 = 23.93 h), the corresponding modulation depth z as 10 km, and contemporary velocity of the plate motion (V_L) for Blanco ridge Transform Fault as 56 mm/yr respectively (Wilson, 1993). The observations from the analysis are shown in Fig. 8 where we can observe the values of ε, d_c, T/T_c, R/R_c, and C as a function of A. The parameter $A = a\sigma_*$, where a is the rate-and-state dependent frictional parameter, determined from the rock friction experiments in the laboratory (Marone, 1998). Its value ranges from $10^{-4} - 10^{-2}$ (Marone, 1998). σ_* is the effective normal stress. The cost function C can be expressed as:

$$C = \sqrt{\frac{\left(1 - \frac{T}{T_c}\right)^2 + \left(1 - \frac{R}{R_c}\right)^2}{2}} \quad (5)$$

Where, critical period of external stress perturbation (T_c), the period of external stress perturbation (T), critical dimension of the slipping zone (R_c) and dimension of the slipping zone (R).

The red circles in each panel are the best-fit model parameters and blue circle ranges are values, with considerably low cost function (Fig. 8). The panels in Fig. 8 show only lesser values for cost function C represented by the limited range of A. Also, we have observed that, the

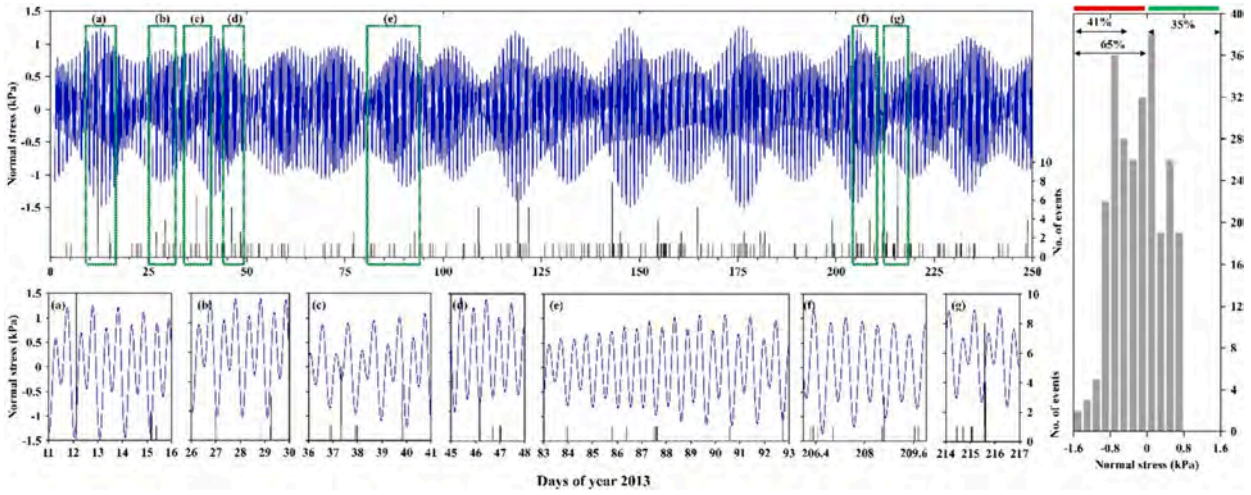

Fig. 7. Representative time series of tidal Normal stress (Ocean tidal loading) variations at the Blanco transform fault and deeper (7–15 km) seismicity histogram of hourly bins showing the correlation of events with low tidal stress amplitudes (highest amplitude compression) during diurnal, monthly and fortnighly stress perturbations. Inset histogram of corresponding stress values of each events shows a higher distribution of events (41 %) during lower amplitude negative tidal stress than total negative tidal stress (65 %).

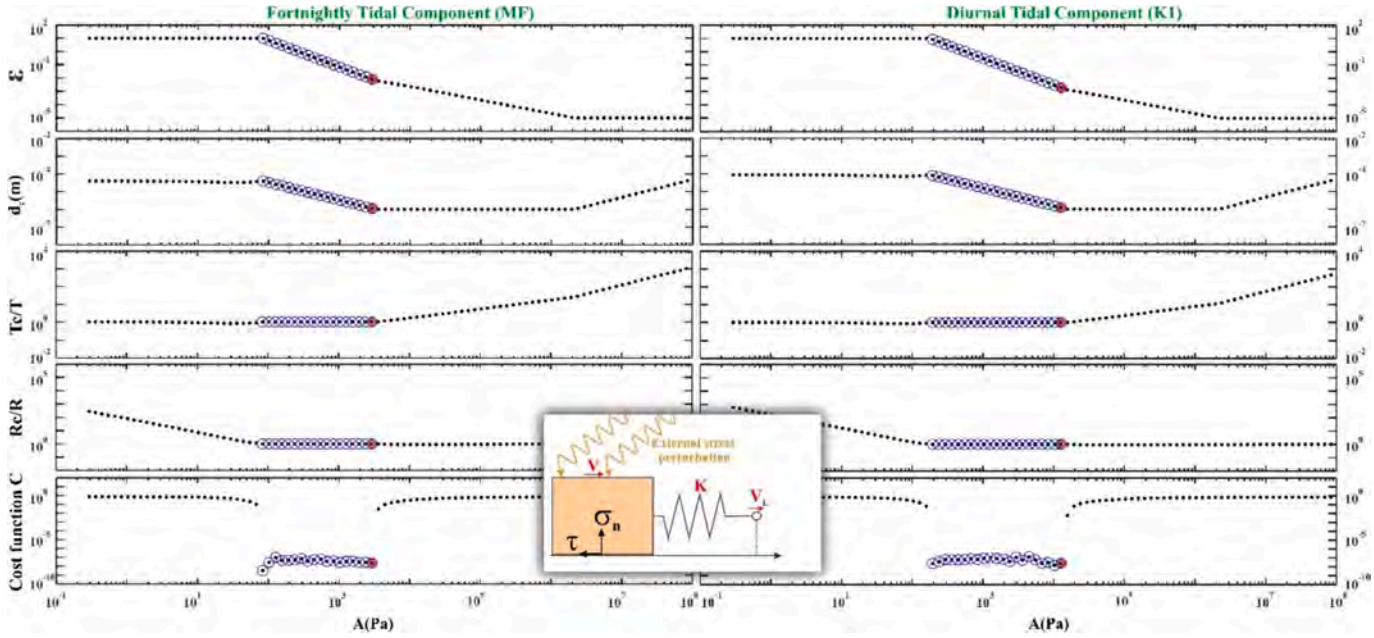

Fig. 8. Variations of the resonance parameters of $\frac{T}{T_c}$, $\frac{R_c}{T}$ and C considering semi-diurnal and diurnal periods through a function of the A parameter. The red square symbols and blue circle symbols are best-fit parameters and the range of values from accepted model respectively (Table 1). We considered forcing fortnightly period $T = 13.66$ days (i.e., MF Tidal constituent) and Diurnal period $T = 23.93$ h (i.e., K1 Tidal constituent),characteristic slipping zone size $R = 2$ km, depth (z) =10 km and loading velocity $V_L = 56$ mm/year. Inset shows a schematical representation of the single block where an external stress perturbation acting on the block moving on a plane with velocity V and pulled by the loading velocity V_L. The stiffness of the spring k, normal stress (σ_n) and shear stress (τ) on the plane. (For interpretation of the references to colour in this figure legend, the reader is referred to the web version of this article.)

d_c parameter supports the range of variations in a very narrow domain i. e. from 10^{-6} to 10^{-5} m (Fig. 8, Fig. 9, Table 1). Further, the estimated value of d_c is consistent with the laboratory value of d_c derived from the rock friction experiments (Marone, 1998). ε was varying roughly in the range 7×10^{-3} to 2×10^{-3} (Fig. 8, Fig. 9, Table 1). As $\frac{b}{a} = 1 + \varepsilon$, we can state that $\frac{b}{a}$ is near to 1. From the resonance theory it is also accepted that resonance destabilization can become sensitive only at the fault segments in neutral stability zone (i.e., where b > a and a ≈ b). Now, following the framework of rate-and-state friction, the region is believed to be in a velocity neutral zone which can be defined as a stability boundary or transition boundary present between regions of active seismicity and mostly aseismic (Scholz et al., 2019).

Further, the parameters V_L, T, R, and z are strategically varied, considering natural values of contemporary plate velocity (V_L) which is suggested to be ranging in the values 0.1 to 100 mm/yr (Gordon, 1998; Zatman et al., 2001), and modulation periods of perturbation (T), which are again in the range of 0.001 to 10 years (Senapati et al., 2022). We have assumed the zone of slipping of fault portion (R) and depth (z) as 2 km and 10 km, respectively according to the seismicity present in the zone. In Fig. 9, the domains of resonance destabilization are characterized by $\frac{T}{T_c} \rightarrow 1$, $\frac{R}{Rc} \rightarrow 1$, where the cost function (C) value is also minimum. Following this, we have marked the regions of possible destabilization

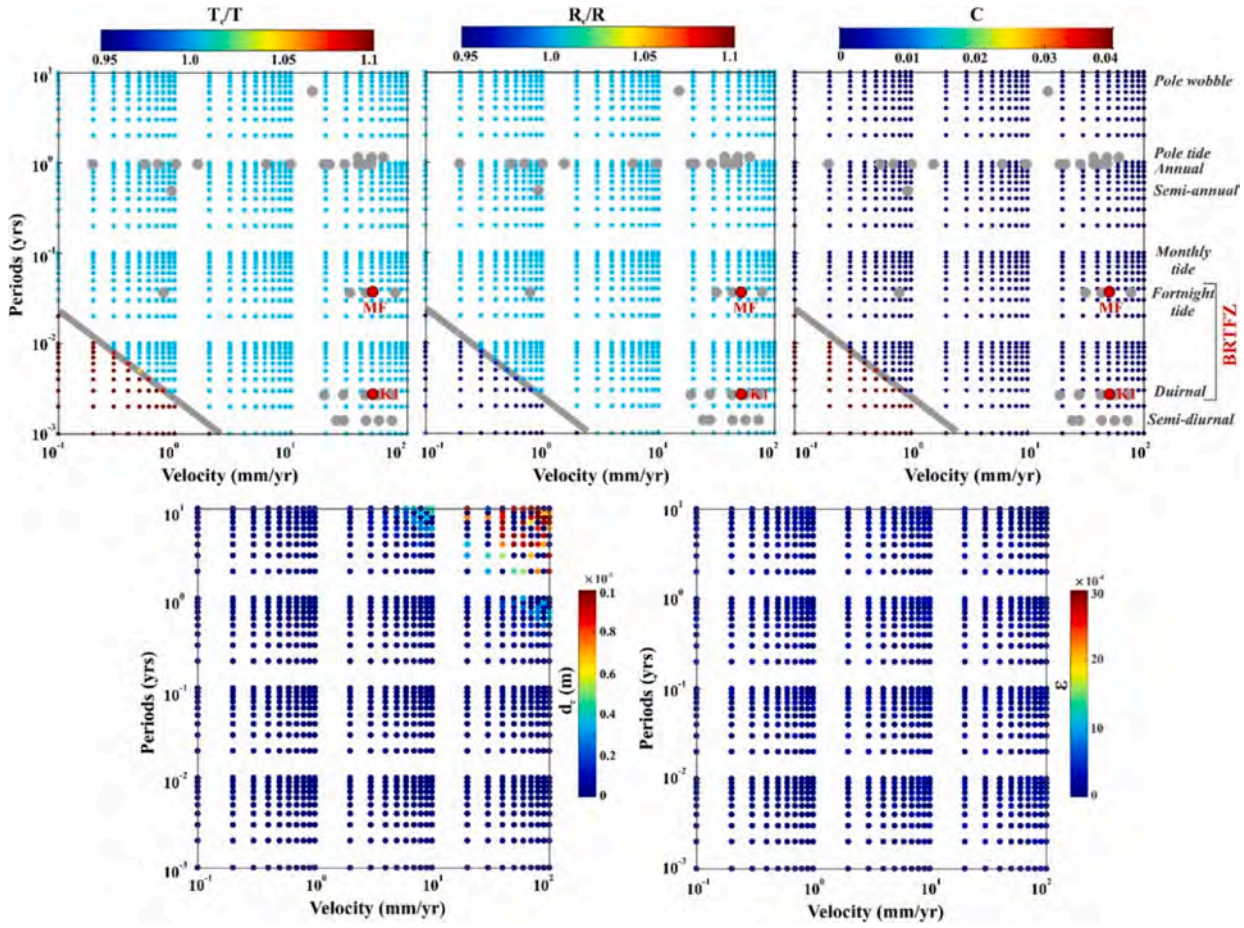

Fig. 9. (*Top panel*) Variation in the parameters of the fault resonance that are estimated to have resulted from the destabilization process in the presence of rate-and-state dependent friction. The gray line served as a dividing line between the zone of potential resonance instability and the zone of no potential resonance destabilization. With the decrease in the dimension of slipping zone (R) and depth (z), the area of no resonance destabilization zone would also decrease (Senapati et al., 2022). The gray dots represent possible documented destabilization zones and the red dots represent the BRTFZ, which falls under the resonance destabilization zone for diurnal as well as fortnightly tidal modulation. (*Bottom panel*) Variation of dc and ε as a function of stress perturbation period (T) and fault velocity (V_L), considering the same parameters of R and z. (For interpretation of the references to colour in this figure legend, the reader is referred to the web version of this article.)

for each V_L vs. T plot (i.e., denoted by the represented gray lines in Fig. 9). From the comparisons, it is suggested that the stress perturbations due to tidal loading can modulate the seismicity at BRTFZ by the mechanism of resonance destabilization.

Moreover, the parameter $A = a\sigma^*$ varies in the particular range of 10^3–10^4 Pa (Fig. 8, Table 1). From that, we have calculated the effective normal stress as $\sigma_* = \frac{A}{a}$, where $a = 10^{-4}$–10^{-2} derived from laboratory experiments (Marone, 1998). It has been observed that the effective normal stress is very low as compared to the lithostatic stress (Table 1), which suggests of high pore-fluid pressure in the BRTFZ. Therefore, we can also infer that the hydrothermal circulation process in the fluid-rich serpentinized mantle makes the respective segments conditionally stable (i.e., falling under neutral stability), hence making this crust-mantle transition segment of the BRTFZ marginally sensitive towards the periodic tidal stress perturbation. Hence, we suggested that the mechanism of resonance destabilization is a favorable mechanism for the tidal triggering and seismicity modulation at this frictional transition zone (Fig. 8).

5. Discussions

5.1. High b-values in GR-law

The relatively low b-values associated with the seismicity in the shallow crust or un-clustered seismicity (Fig. 4) suggest that it is dominated by the larger magnitude of earthquake populations, as compared with the mantle, which is dominated by smaller magnitude (Fig. 4) (Kuna et al., 2019). All recorded five events of $M_L > 4.5$, including January 30, 2013, of M_L5.5 earthquake occurred at the shallow depth (0–7 km) in the oceanic crust however, smaller magnitude seismic swarms are dominated at the deeper depth (7-15 km) in the mantle. At the BRTFZ, our observations regarding b-values for seismic swarms are considered to be relatively higher (1.12 ± 0.11 for seismic swarms and 1.29 ± 0.15 for deeper swarms), which supports the global values of swarms at active hydrothermal systems (Francis, 1968, 1974; Hill, 1977; Wiemer and McNutt, 1997; Kundu et al., 2012). It is also observed that the shallow seismic swarms have a comparatively lower b-value (0.88 ± 0.15) than the deeper swarms which is also consistent with the values in previous reports (Kuna et al., 2019). Although the uncertainties in the b-values can determine the actual range of the values that might range around the values of 1–1.25 for the seismic swarms and 1.1–1.5 for the deeper seismic swarms, the b-values still remain on the higher side of the smaller magnitude distribution. Also, considering the uncertainties values of the shallow swarms, it can actually range between 0.7 and 1, which is closer to the lower thresholds of the b-value ranges for all swarms and deeper swarms (i.e., 1 and 1.1, respectively). However, the higher b-values for the deeper seismic swarms can certainly be considered to be on the higher side despite the

Table 1
Best fit and range of acceptable parameters (columns 2 and 3). Column 5 is the lithostatic stress (σ_{litho}) from average 3000 kg/m^3 dense oceanic crust, $\sigma_* = \frac{A}{a}$ from column 2 and taking a = 10^{-4} – 10^{-2}. The $\frac{\sigma_*}{\sigma_{litho}}$ is the effective normal stress to lithostatic stress ratio. Note, σ_* is some magnitudes lower compared to σ_{litho}, which indicates high pore fluid pressure. In this tidal induced fault resonance model, we considered fortnightly and diurnal forcing periods (i.e., MF and K1 component respectively), R = 2 km, z = 10 km and V_L = 56 mm/year which are the effective radius, depth and loading velocity respectively.

Best fit parameters	Best fit Value	Range of acceptable value	Stress parameters	Calculated stress value
Fortnightly Period (MF)				
$\epsilon = \frac{b}{a} - 1$	7.640 × 10^{-3}	1.968 × 10^{-3}–9.41	σ_{litho} (MPa)	2.943 × 10^2
d_c (m)	1.091 × 10^{-6}	1.091× 10^{-6}–3.829× 10^{-5}	σ_* (MPa)	0.2943–29.43
$A = a\sigma_*$ (Pa)	2.943 × 10^3	83.8–2.943 × 10^3	$\frac{\sigma_*}{\sigma_{litho}}$	1× 10^{-3}–1× 10^{-1}
Diurnal Period (K1)				
$\epsilon = \frac{b}{a} - 1$	2.305 × 10^{-3}	2.305 × 10^{-3}–9.98	σ_{litho} (MPa)	2.943 × 10^2
d_c (m)	1.0.553 × 10^{-6}	1.091× 10^{-6}–7.601× 10^{-5}	σ_* (MPa)	1.033–103.3
$A = a\sigma_*$ (Pa)	1.033 × 10^4	1.570 × 10^2–1.033 × 10^4	$\frac{\sigma_*}{\sigma_{litho}}$	3.51× 10^3–3.51× 10^{-1}

uncertainties. This confirms the presence of a high number of lower-magnitude events in the deeper swarms observed at the crust-mantle boundary zone.

On the other hand, various hypotheses are widely proposed for the explanation of higher b-values in the GR-law. The higher b-value may be attributed to various phenomena and hypothesis which include higher fluid and temperature activities (Warren and Latham, 1970; Kundu et al., 2012), nature of the corresponding rock materials in structure (e.g., higher b-values are observed in a ductile rock rather than a brittle rock) or may be the materials subjected to the respective mechanical loading being highly heterogeneous (Mogi, 1962) or else amplitude decrease of the corresponding stress field (Scholz, 1968). However, at the BRTFZ, higher b-values (1.29 ± 0.15) are observed in the deeper seismic swarms compared to the shallow region (0.88 ± 0.15). Therefore, it is assumed that, in the deeper region at BRTFZ, the serpentinization of mantle peridotites offers a brittle-ductile transition zone that provides sufficient permeability for the hydrothermal circulation of fluids for generation of a higher number of low-magnitude seismic swarms.

5.2. Dominance of diurnal tidal periodicity and possible explanations

The seismic swarms that occurred deeper at the mantle and brittle-ductile transition zone appear to be tidally sensitive; however, the significance of semi-diurnal M2 tidal periodicity is absent in the present study region (Fig. 5). The absence of semi-diurnal component though can be explained with the amplitude variance of tidal forcing by different major tidal components (Barreyre et al., 2014). Moreover, the semi-diurnal tidal cycles contain alternate low and high amplitude tidal cycles, which appears during a diurnal period. So, it is also acceptable the seismicity triggered during the high amplitude tidal cycles can possibly show strong diurnal periodicity (Wilcock, 2009).

It has been reported that there is an enhanced hydrothermal activity during higher hydrostatic pressure condition at the ocean bottoms (Jupp and Schultz, 2004). Here, the fluid flow depends on the contrast of pore fluid pressure and confining pressure (lithostatic/hydrostatic) i.e. effective pressure. The fluid flow occurs when the confining pressure is near hydrostatic pressure experiencing decompression from diurnal tidal relaxation and the brittle deformation takes place when the confining pressure is near to the lithostatic pressure during the high amplitude diurnal tidal compressions (Glasby and Kasahara, 2001). The contrast among the confining pressure (lithostatic and hydrostatic) increases with depth and is highest at the brittle-ductile transition zone which indicates the zone of highest effective pressure for fluid flow under tidal decompression (Sohn et al., 1995).

From the observed N_{ex} values of FNS, RLSS and CFS (Fig. 6), we can infer that the extensional normal stress indicated a dilatation which may have reduced the crack closure level and facilitated the movement of fluid into the crack. This leads to a temporary increase of the effective pore pressure under compressional stress conditions and consequently increased the fluid flux and diffusion at the serpentinized mantle or crust-mantle transition along the fault plane. The seismic swarms at the brittle-ductile transition zone of oceanic transform faults are also believed to be produced from the aseismic slip (Liu et al., 2020; Kuna et al., 2019; McGuire, 2019). The deeper zone is believed to be in aseismic slip or creep movement which generate the swarms at the asperities present in the transition zone (Kuna et al., 2019). Moreover, the presence of increasing fluid flux and effective fluid pressure due to the tidal compressions, made this frictional transition zone conditionally stable sliding (i.e., velocity weakening to velocity strengthening friction), promoting the transient slip and the occurrence of seismic swarms. The seismic swarm, thus, can become more sensitive to tidal stress perturbation. Previously, it has been also reported that the aseismic slips are encouraged by the dilatation of the slip zone due to the increase in pore-spaces from particle rotations and hydrothermal circulations (Liu et al., 2020; Kuna et al., 2019). However, the presence of tidal periodicity and strong tidal correlation of only the deeper seismic swarms gives an indication of the effect of tidal stress perturbations.

Further, in high pore fluid pressure conditions, the incremental pressure due to compressions from tidal loading drives a flux of interstitial fluid according to Darcy's law in the permeable host or the serpentinized mantle (Jupp and Schultz, 2004). The pressure exerted by the tidal forcing, hence modulates the flow of hydrothermal fluid in the brittle-ductile transition zone that conditionally promotes the seismic swarms. The pressure generated by tidal forcing is highest during the highest tidal compressions during the higher amplitude of the low tidal cycles, which is around 0.5–1 kPa higher during the diurnal perturbation period as compared to the semi-diurnal perturbation period (Fig. 7). Tidal modulations in buoyancy derived hydrothermal flow require pressure modulation of as less as 0.02 MPa, which can be produced by the tides under different perturbation periods (Glasby and Kasahara, 2001). It is also noticeable that the major distribution of the events in the deeper swarms is during the higher amplitude low tidal cycles (higher compression during higher amplitudes of low tides) (Fig. 7). Therefore, the incremental pressure during the higher compressions from diurnal perturbations highly influences the flow of hydrothermal fluids that modulate the occurrence of seismic swarms.

The swarms at the BRTFZ are probably clustered around the small asperities present in the transitional zone (Kuna et al., 2019). The swarms being very similar in nature show similar number of events for each cluster. In this study, we have treated the whole catalog of the swarms as a group for the tidal analysis as we focus on the tidal responsiveness of the events, thereby supporting our hypothesis of the tidal correlation of deeper events, which probably results from the continuous aseismic slip or creep (Kuna et al., 2019). Nevertheless, we also acknowledge that analyzing the clustered swarms as a single group without discrimination of timeframe or particular zone of occurrence (e.g. around barrier zones in Liu et al., 2020) may have suppressed or influenced the tidal signatures. This also recommends that we can expect variable tidal signatures for individual cluster of swarms (Thomas et al., 2012) that can provide some idea about the associated asperity characteristics. Still, for the respective study we have focused on the swarms as a group that occur in the deeper part (i.e. deeper than the transitional zone at the depth of 7kms). Therefore, we have stuck to the idea of

finding the tidal responsiveness of the deeper swarms and focused on the swarms as a single group. In contrast, at the deeper depths, it is difficult to generate unstable slip on the small asperities. So, this improvisation would require additional statistical and observational analysis for a clear idea. However, based on the established tidal statistical analyses it is not recommended to check the correlations based on the small number of events for each cluster, but we have also checked for the single cluster characteristics but we did not find any significant difference in the cluster characteristics. Therefore, it is difficult to comment on the dominance of the individual clusters on the overall results.

5.3. Fault resonance and critical triggering threshold in support of diurnal modulations

The fault resonance destabilization model only explains the essential conditions required for the destabilization of a fault system by the tidal resonance process. However, this model does not explain for respective period of excitation (T) for which the fault system is more sensitive to the resonance process. Therefore, to quantify the sensitivity of the fault system to the resonance process for different periods of excitation, we have estimated the CFS induced by FNS and RLSS perturbations, which is expressed as (Senapati et al., 2023b, 2024):

$$|\Delta CFS| = \left| \frac{\frac{q}{q_c}\mu_{ss}\sigma_1 - \tau_1}{\frac{k}{k_c}} \right| \times \sqrt{\frac{\left(\frac{q}{q_c}\right)^2 + q_c^2}{\left(1 - \left(\frac{q}{q_c}\right)^2 \frac{k_c}{k}\right)^2 + q^2\left(1 - \frac{k_c}{k}\right)^2}} \quad (6)$$

We have considered periods of excitation as 23.93 h and 12.42 h (i.e., periodicities associated with the BRTFZ), d_c as 10^{-6} m, μ_{ss} as 0.3, (b-a) as 10^{-4} and V_L as 56 mm/yr (Wilson, 1993) and estimated the CFS induced by tidal stress perturbations (Fig. 10). It has been suggested that the amplitude of ΔCFS is greatest around T_c when k is close to k_c (Fig. 10). The modeling suggests, ΔCFS is greatest at diurnal tidal phase (23.93 h) as compared with the semi-diurnal tidal phase (12.42 h) which is also consistent with our tidal periodicity results (Fig. 5). Hence, we suggest that, the presence of serpentinized mantle and circulation of hydrothermal fluids in the deeper BRTFZ makes it more susceptible for seismicity modulation by the fault resonance process. The modeling results also support the strong diurnal periodicity of seismicity associated with the deeper BRTFZ.

Furthermore, the critical value of stress perturbation due to external stress is also important for understanding seismicity modulation. It is suggested that triggering of an event due to external stress occurs during the build-up of tectonic stress and well defined critical stress values (Rydelek et al., 1992; Curchin and Pennington, 1987; Emter, 1997). Further, the critical threshold values for modulations by tidal stress perturbation range in about 0.002 MPa to 0.004 MPa for coulomb failure stress under experimental conditions (Beeler and Lockner, 2003), and under observations from reported tidal modulations as 0.15–0.3 kPa for shear stress (Thomas et al., 2009), more than 0.7 kPa for normal stress (Stroup et al., 2007). However, Ziv and Rubin (2000) suggested that, there is no lower threshold existing for earthquake triggering. Although the external tidal stress perturbation during different tidal periods at the BRTFZ is relatively low, it is also sufficient to destabilize the fault system by fault resonance process and modulate the seismicity to exhibit the variations in the periodicity of the seismicity (Fig. 11).

5.4. Comparison with global tidal modulations

In the last decade, tidal modulations of seismicity have been reported around the world in different tectonic settings and geographic locations, e.g., seismicity at the Axial seamount of Juan de Fuca Mid oceanic ridge (Wilcock, 2001; Scholz et al., 2019; Sahoo et al., 2021), Volcanic tremors at Campi Flegrei caldera (Petrosino et al., 2018), Tremors at Cascadia subduction zone (Cochran et al., 2004; Tanaka et al., 2006; Thomas et al., 2009), seismicity at East pacific rise (Wilcock, 2009; Tolstoy et al., 2002; Tan et al., 2018), etc. In most of these cases, the strongest semidiurnal tidal periodicity (i.e., M2) is observed as the significant periodicity. However, the diurnal and fortnightly tidal periodicity has also been reported in Campi Flegrei caldera, TAG hydrothermal field of the Mid-Atlantic Ridge, San Andreas fault, East Pacific Rise etc. (Bhatnagar et al., 2016; Petrosino et al., 2018; van der Elst et al., 2016; Glasby and Kasahara, 2001). Moreover, The presence of diurnal periodicity in the seismicity associated to submarine hydrothermal systems is influenced by several factors i.e., effect of fluid flow along fault zones (Glasby, 1998; Sibson et al., 1975) effect of compression and dilatation of micro-cracks due to tidal effect (Prioul et al., 2000), effect of the

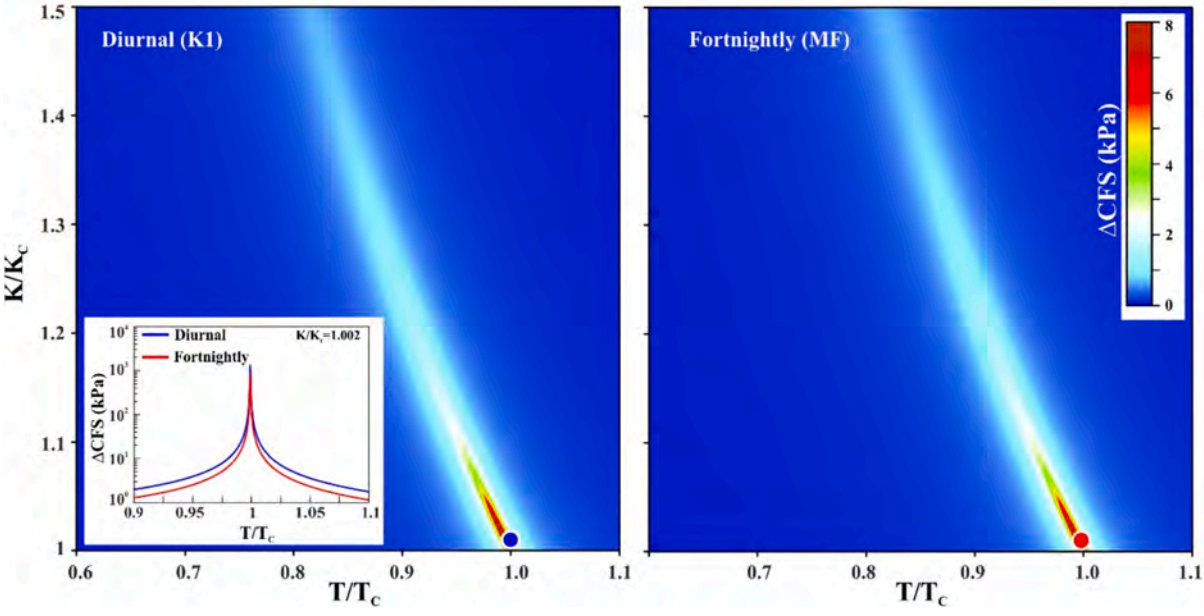

Fig. 10. Variation of Coulomb failure stress change (ΔCFS) as a function of normalized periods of excitation (T/Tc) and normalized fault stiffness (k/kc) for diurnal, fortnightly, tidal phases, respectively. Blue circle and red circle indicates the respective points of ΔCFS profiles for diurnal (K1) and fortnightly (MF) periods, that are shown as inset figures. (For interpretation of the references to colour in this figure legend, the reader is referred to the web version of this article.)

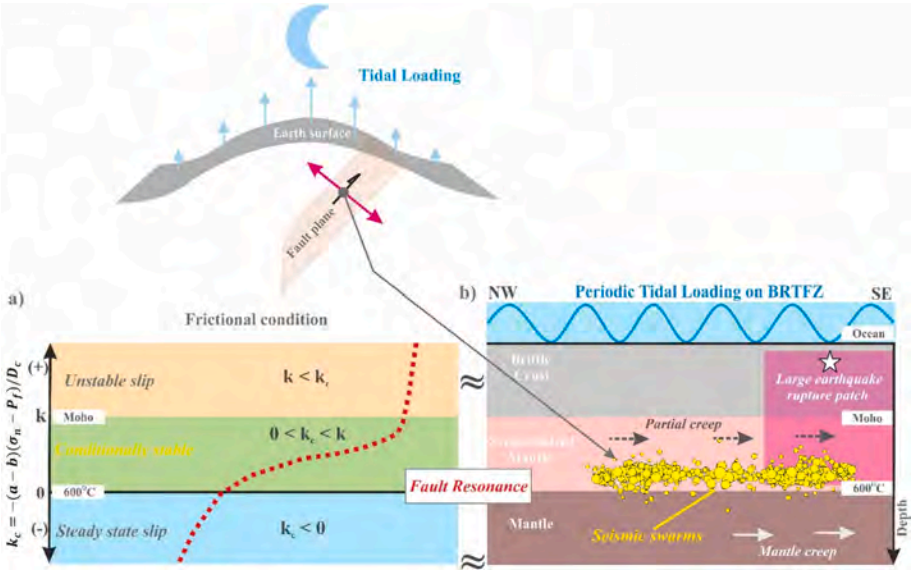

Fig. 11. Schematic representation of the occurrence of seismicity/seismic swarm along the Blanco Ridge Transform Fault Zone (BRTFZ), frictional condition and possible modulation by the tidal stress perturbations at the serpentinized mantle and associated brittle crust zone. (a) Shows variation of fault stiffness (k) with depth. (b) Shows the vertical cross-section along the Blanco Ridge Transform Fault Zone (BRTFZ). Seismic swarms are mainly concentrated along the crust-mantle transition boundary, which corresponds to the conditionally stable frictional segment. Tidal attraction induces periodic displacements on the Earth's surface leading to high vertical stress variations on the fault plane and making the transition boundary (or conditionally stable zone) more sensitive to external tidal stress oscillations and seismicity modulation.

physical and chemical parameters of the hydrothermal fluid (Shock, 1992), effects of tidal loading on the temperature of diffuse hydrothermal flow (Little et al., 1988) etc. The dilatation and compression of the oceanic crust due to the tides may increase the diameter of the pores and fissures of the ocean crust and significantly change the rate of flow of the hydrothermal fluid and modulate the seismicity. Moreover, the pressure from rising magma, degassing of magma and associated fault orientations may also be crucial for seismicity modulations (Glasby and Kasahara, 2001). Therefore, we suggest that the high amplitude diurnal stress perturbations cause dilatation and compression of the oceanic crust, which may increase the diameter of the pores and fissure of the serpentinized mantle and significantly increase the fluid flux to modulate the seismicity at deeper seismic swarms of the BRTFZ. We have also acknowledged that the fault orientation, pressure and gas content of the hydrothermal system also play an important role in seismicity modulation at BRTFZ.

6. Conclusions

From this robust analysis, our study concludes with the following key statements :

1. The seismicity associated with the Blanco Ridge Transform Fault Zone (BRTFZ) at deeper depth (7–15) exhibits strong diurnal tidal and a weak fortnightly periodicity with higher seismic b-values. This indicates the effect of magmatic (or hydrothermal) fluid circulation at this depth (i.e., crust-mantle transition zone).
2. The deeper seismic swarm appears to be very sensitive to the effective tidal normal stress on the fault plane (FNS) at higher percentages of negative N_{ex} (compressive) and higher percentages of positive N_{ex} of shear stress (RLSS). The Coulomb failure stress (CFS) with corresponding encouraging or positive N_{ex} percentages imparts effective unclamping on the fault plane system.
3. The higher amplitude of ΔCFS induced by the FNS and RLSS perturbation for the diurnal period as compared to the semi-diurnal period possibly explains the dominance of diurnal periodicity at the BRTFZ.
4. During the decompression at extensional (positive) stress, the host rock undergoes a dilatation which may reduce the crack closure level and assist the fluid movement. Further, Higher compressions during high amplitude low tidal cycles raise the tidal CFS and effective pore pressure, making fault portions conditionally stable and this crust-mantle transition portion of the BRTFZ more susceptible to periodic tidal stress perturbation. Thus, the process of destabilization due to fault resonance appears as a favorable mechanism for BRTFZ tidal triggering and seismicity modulation.

Datasets and codes availability

Topographic map presented in Fig. 1 has been generated using the General Bathymetric Chart of the oceans by rectangular area search with GeoTIFF output (https://download.gebco.net/). The tidal stress is computed using SPOTL: Some Programs for Ocean-Tide Loading, SIO Technical Report, Scripps Institution of Oceanography(Agnew, 2012) (version 3.3.0.2 URL: https://igppweb.ucsd.edu/~agnew/Spotl/spotlmain.html). The Figs are generated by Grapher graphical application (version 8.7.844 URL: https://www.goldensoftware.com/products/grapher), Surfer graphical application (version 8.7.844 URL: https://www.goldensoftware.com/products/surfer), Generic Mapping Tools (Wessel et al., 2019)(version 5.2.1; URL: https://www.generic-mapping-tools.org/) and Corel Draw graphical application (version 18; URL: https://www.coreldraw.com/en). The seismicity catalog was taken from the original representation in the published article by Kuna et al. (2019) (doi:https://doi.org/10.1038/s41561-018-0287-1), which is an OBS dataset archived at the IRIS Data Management System (http://www.iris.edu).

CRediT authorship contribution statement

Sambit Sahoo: Writing – original draft, Methodology. **Batakrushna Senapati:** Methodology, Investigation. **Dibyashakti Panda:** Methodology, Investigation, Formal analysis. **Shuanggen Jin:** Writing – review & editing, Conceptualization. **Bhaskar Kundu:** Writing – review & editing, Writing – original draft, Conceptualization.

Declaration of competing interest

The authors declare that they have no known competing financial interests or personal relationships that could have appeared to influence the work reported in this paper.

Data availability

Data will be made available on request.

Acknowledgment

The presented work in the article has been performed within the framework of Sambit Sahoo's Ph.D. thesis at NIT Rourkela. We thank John L. Nábělek for providing the original seismicity catalog from the BRTFZ. BS is supported by NITR research fellowship. SS is supported by CSIR-UGC fellowship. We also thank to the Ministry of Earth Sciences (Seismology Division), Govt. of India, as the work is also financially supported through grant number (MoES/P·O(Seismo)/1(349)/2018) to Bhaskar Kundu. We would also like to thank the Editor Dr. Ana Ferreira, and the reviewer Dr. Miguel Neves for constructive comments and suggestions, which significantly improved the quality of the manuscript.

References

Ader, T.J., Lapusta, N., Avouac, J.-P., Ampuero, J.-P., 2014. Response of rate-and-state seismogenic faults to harmonic shear-stress perturbations. Geophys. J. Int. 198, 385–413. https://doi.org/10.1093/gji/ggu144.

Agnew DC. (1996). SPOTL: some programs for ocean-tide loading. SIO ref. Ser. 96–8. *Scripps Instit of Oceanogr, La Jolla, calif*, *35*.

Agnew, D.C., 1997. NLOADF: a program for computing ocean-tide loading. J. Geophys. Res. 102, 5109–5110. https://doi.org/10.1029/96JB03458.

Agnew, D., 2012. SPOTL: Some Programs for Ocean-Tide Loading (SIO Technical Report), Scripps Instit of Oceanogr. University of California. https://escholarship.org/uc/item/954322pg.

Aki, K., 1965. Maximum likelihood estimate of b in the formula log N = a-bM and its confidence limits. Bull. Earthq. Res. Inst. Tokyo Univ. 43, 237–239.

Atef, A.H., Liu, K.H., Gao, S.S., 2009. Apparent Weekly and daily earthquake periodicities in the Western United States. Bull. Seismol. Soc. Am. 99, 2273–2279. https://doi.org/10.1785/0120080217.

Barreyre, T., Escartín, J., Sohn, R.A., Cannat, M., Ballu, V., Crawford, W.C., 2014. Temporal variability and tidal modulation of hydrothermal exit-fluid temperatures at the lucky strike deep-sea vent field, mid-Atlantic ridge. J. Geophys. Res. Solid Earth 119, 2543–2566. https://doi.org/10.1002/2013JB010478.

Beeler, N.M., Lockner, D.A., 2003. Why earthquakes correlate weakly with the solid earth tides: effects of periodic stress on the rate and probability of earthquake occurrence. J. Geophys. Res. 108, 2391. https://doi.org/10.1029/2001JB001518.

Bhatnagar, T., Tolstoy, M., Waldhauser, F., 2016. Influence of fortnightly tides on earthquake triggering at the East Pacific rise at 9°50′N. J. Geophys. Res. Solid Earth 121, 1262–1279. https://doi.org/10.1002/2015JB012388.

Boettcher, M.S., 2004. Effects of normal stress variation on the strength and stability of creeping faults. J. Geophys. Res. 109, B03406 https://doi.org/10.1029/2003JB002824.

Braunmiller, J., Nábělek, J., 2008. Segmentation of the Blanco transform fault zone from earthquake analysis: complex tectonics of an oceanic transform fault. J. Geophys. Res. 113, B07108 https://doi.org/10.1029/2007JB005213.

Cochran, E.S., Vidale, J.E., Tanaka, S., 2004. Earth tides can trigger shallow thrust fault earthquakes. Science 306, 1164–1166. https://doi.org/10.1126/science.1103961.

Curchin, J.M., Pennington, W.D., 1987. Tidal triggering of intermediate and deep focus earthquakes. J. Geophys. Res. Solid Earth 92 (B13), 13957–13967. https://doi.org/10.1029/JB092iB13p13957.

De Lauro, E., De Martino, S., Falanga, M., Petrosino, S., 2013. Synchronization between tides and sustained oscillations of the hydrothermal system of Campi Flegrei (Italy): hydrothermal tremor at Campi Flegrei. Geochem. Geophys. Geosyst. 14, 2628–2637. https://doi.org/10.1002/ggge.20149.

Díaz, J., Ruiz, M., Sánchez-Pastor, P.S., Romero, P., 2017. Urban seismology: on the origin of earth vibrations within a city. Sci. Rep. 7, 15296 https://doi.org/10.1038/s41598-017-15499-y.

Dieterich, J.H., 1987. Nucleation and triggering of earthquake slip: effect of periodic stresses. Tectonophysics 144 (1–3), 127–139. https://doi.org/10.1016/0040-1951(87)90012-6.

Egbert, G.D., Erofeeva, S.Y., 2002. Efficient inverse modeling of Barotropic Ocean tides. J. Atmos. Ocean. Technol. 19, 183–204. https://doi.org/10.1175/1520-0426(2002)019<0183:EIMOBO>2.0.CO;2.

Embley, R.W., Wilson, D.S., 1992. Morphology of the Blanco transform fault zone-NE Pacific: implications for its tectonic evolution. Mar. Geophys. Res. 14, 25–45. https://doi.org/10.1007/BF01674064.

Emter, D., 1997. Tidal triggering of earthquakes and volcanic events. Tidal Phenomena 293-309. https://doi.org/10.1007/BFb0011468.

Farrell, W.E., 1972. Deformation of the earth by surface loads. Rev. Geophys. 10, 761. https://doi.org/10.1029/RG010i003p00761.

Francis, T.J.G., 1968. The detailed seismicity of mid-oceanic ridges. Earth Planet. Sci. Lett. 4, 39–46. https://doi.org/10.1016/0012-821X(68)90051-4.

Francis, T.J.G., 1974. A new interpretation of the 1968 Fernandina caldera collapse and its implications for the mid-oceanic ridges. Geophys. J. Int. 39, 301–318. https://doi.org/10.1111/j.1365-246X.1974.tb05456.x.

Glasby, G.P., 1998. The relation between earthquakes, faulting, and submarine hydrothermal mineralization. Mar. Georesour. Geotechnol. 16 (2), 145–175.

Glasby, G.P., Kasahara, J., 2001. Influence of tidal effects on the periodicity of earthquake activity in diverse geological settings with particular emphasis on submarine hydrothermal systems. Earth Sci. Rev. 52, 261–297. https://doi.org/10.1016/S0012-8252(00)00031-3.

Gordon, R.G., 1998. Plate nonrigidity, diffuse plate boundaries, and global plate reconstructions. Annu. Rev. Earth Planet. Sci. 26, 615–642. https://doi.org/10.1146/annurev.earth.26.1.615.

Goulty, N.R., 1979. Tidal triggering of deep moonquakes. Phys. Earth Planet. Inter. 19 (1), 52–58. https://doi.org/10.1016/0031-9201(79)90089-X.

Gutenberg, B., Richter, C.F., 1944. Frequency of earthquakes in California. Bull. Seismol. Soc. Am. 34 (4), 185–188. https://doi.org/10.1038/156371a0.

Heaton, T.H., 1975. Tidal triggering of earthquakes. Geophys. J. Int. 43, 307–326. https://doi.org/10.1111/j.1365-246X.1975.tb00637.x.

Heimisson, E.R., Avouac, J., 2020. Analytical prediction of seismicity rate due to tides and other oscillating stresses. Geophys. Res. Lett. 47 https://doi.org/10.1029/2020GL090827.

Hill, D.P., 1977. A model for earthquake swarms. J. Geophys. Res. 82, 1347–1352. https://doi.org/10.1029/JB082i008p01347.

Jupp, T.E., Schultz, A.A., 2004. Poroelastic model for the tidal modulation of seafloor hydrothermal systems. J. Geophys. Res. 109, B03105 https://doi.org/10.1029/2003JB002583.

Kuna, V.M., Nábělek, J.L., Braunmiller, J., 2019. Mode of slip and crust–mantle interaction at oceanic transform faults. Nat. Geosci. 12, 138–142. https://doi.org/10.1038/s41561-018-0287-1.

Kundu, Bhaskar, Legrand, Denis, Gahalaut, Kalpna, Gahalaut, Vineet K., Mahesh, P., Kamesh Raju, K.A., Catherine, J.K., Ambikapthy, A., Chadha, R.K., 2012. The 2005 volcano-tectonic earthquake swarm in the Andaman Sea: triggered by the 2004 great Sumatra-Andaman earthquake. Tectonics 31. https://doi.org/10.1029/2012TC003138.

Lammlein, D.R., 1977. Lunar seismicity and tectonics. Phys. Earth Planet. Inter. 14, 224–273. https://doi.org/10.1016/0031-9201(77)90175-3.

Little, S.A., Stolzenbach, K.D., Grassle, F., 1988. Tidal current effects on temperature in diffuse hydrothermal flow: Guyamas Basin. Geophys. Res. Lett. 15, 1491–1494. https://doi.org/10.1029/GL015i013p01491.

Liu, Y., McGuire, J.J., Behn, M.D., 2020. Aseismic transient slip on the Gofar transform fault, East Pacific rise. Proc. Natl. Acad. Sci. 117 (19), 10188–10194. https://doi.org/10.1073/pnas.1913625117.

Lockner, D.A., Beeler, N.M., 1999. Premonitory slip and tidal triggering of earthquakes. J. Geophys. Res. 104, 20133–20151. https://doi.org/10.1029/1999JB900205.

Lognonné, P., 2005. Planetary seismology. Annu. Rev. Earth Planet. Sci. 33, 571–604. https://doi.org/10.1146/annurev.earth.33.092203.122604.

Lowrie, W., 2011. A Student's Guide to Geophysical Equations. Cambridge University Press.

Lowry, A.R., 2006. Resonant slow fault slip in subduction zones forced by climatic load stress. Nature 442, 802–805. https://doi.org/10.1038/nature05055.

Manga, M., Beresnev, I., Brodsky, E.E., 2012. Changes in permeability caused by transient stresses: field observations, experiments, and mechanisms. Rev. Geophys. 50 https://doi.org/10.1029/2011RG000382.

Marone, C., 1998. Laboratory-derived friction laws and their application to seismic faulting. Annu. Rev. Earth Planet. Sci. 26, 643–696. https://doi.org/10.1146/annurev.earth.26.1.643.

Matsumoto, K., Sato, T., Takanezawa, T., Ooe, M., 2001. GOTIC2: A Program for Computation of Oceanic Tidal Loading Effect.

McGuire, J.J., 2019. The geology of earthquake swarms. Nat. Geosci. 12 (2), 82–83. https://doi.org/10.1038/s41561-019-0302-1.

McNutt, S.R., Beavan, R.J., 1984. Patterns of earthquakes and the effect of solid earth and ocean load tides at Mount St. Helens prior to the may 18, 1980, eruption. J. Geophys. Res. 89, 3075–3086. https://doi.org/10.1029/JB089iB05p03075.

Métivier, L., de Viron, O., Conrad, C.P., 2009. Evidence of earthquake triggering by the solid earth tides. Earth Planet. Sci. Lett. 278, 370–375. https://doi.org/10.1016/j.epsl.2008.12.024.

Minshull, T.A., Goulty, N.R., 1988. The influence of tidal stresses on deep moonquake activity. Phys. Earth Planet. Inter. 52 (1–2), 41–55. https://doi.org/10.1016/0031-9201(88)90056-8.

Mogi, K., 1962. Study of elastic shocks caused by the fracture of heterogeneous materials and its relation to earthquake phenomena. Bull. Earthq. Res. Inst., Univ. Tokyo 40, 125–173. https://repository.dl.itc.u-tokyo.ac.jp/record/33798/file_preview/ji0401006.pdf.

Panda, D., Kundu, B., Gahalaut, V.K., et al., 2018. Seasonal modulation of deep slow-slip and earthquakes on the Main Himalayan thrust. Nat. Commun. 9, 4140. https://doi.org/10.1038/s41467-018-06371-2.

Perfettini, H., 2000. Frottement Sur Une Faille: Influence des Fluctuations de la Contrainte Normale, Paris. Doctoral dissertation.

Perfettini, H., Schmittbuhl, J., 2001. Periodic loading on a creeping fault: implications for tides. Geophys. Res. Lett. 28, 435–438. https://doi.org/10.1029/2000GL011686.

Perfettini, H., Schmittbuhl, J., Rice, J.R., Cocco, M., 2001. Frictional response induced by time-dependent fluctuations of the normal loading. J. Geophys. Res. 106, 13455–13472. https://doi.org/10.1029/2000JB900366.

Petrosino, S., Dumont, S., 2022. Tidal modulation of hydrothermal tremor: examples from Ischia and Campi Flegrei volcanoes, Italy. Front. Earth Sci. 9, 775269 https://doi.org/10.3389/feart.2021.775269.

Petrosino, S., Cusano, P., Madonia, P., 2018. Tidal and hydrological periodicities of seismicity reveal new risk scenarios at Campi Flegrei caldera. Sci. Rep. 8, 13808. https://doi.org/10.1038/s41598-018-31760-4.

Prioul, I.R., Cornet, F.A., Dorbath, C., Dorbath, L., Ogena, M., Ramos, E., 2000. An induced seismicity experiment across a creeping segment of the Philippine fault. J. Geophys. Res. 105, 13595–13612. https://doi.org/10.1029/2000JB900052.

Ray, R.D., 1999. A Global Ocean Tide Model from TOPEX/POSEIDON Altimetry, vol. GOT99. National Aeronautics and Space Administration, Goddard Space Flight Center, p. 2.

Reasenberg, P., 1985. Second-order moment of Central California seismicity, 1969-1982. J. Geophys. Res. 90, 5479–5495. https://doi.org/10.1029/JB090iB07p05479.

Rydelek, P.A., Sacks, I.S., Scarpa, R., 1992. On tidal triggering of earthquakes at Campi Flegrei, Italy. Geophys. J. Int. 109, 125–135. https://doi.org/10.1111/j.1365-246X.1992.tb00083.x.

Sahoo, S., Kundu, B., Petrosino, S., Yadav, R.K., Tiwari, D.K., Jin, S., 2024. Feedback responses between endogenous and exogenous processes at Campi Flegrei caldera dynamics, Italy. Bull. Volcanol. 86 (3), 22. https://doi.org/10.1007/s00445-024-01719-7.

Sahoo, S., Senapati, B., Panda, D., Tiwari, D.K., Santosh, M., Kundu, B., 2021. Tidal triggering of seismicity associated with caldera dynamics in the Juan de Fuca ridge. J. Volcanol. Geotherm. Res. 417, 107319 https://doi.org/10.1016/j.jvolgeores.2021.107319.

Sahoo, S., Tiwari, D.K., Panda, D., Kundu, B., 2022. Eruption cycles of Mount Etna triggered by seasonal climatic rainfall. J. Geodyn. 149, 101896 https://doi.org/10.1016/j.jog.2021.101896.

Scholz, C.H., 1968. Microfracturing and the inelastic deformation of rock in compression. J. Geophys. Res. 73, 1417–1432. https://doi.org/10.1029/JB073i004p01417.

Scholz, C.H., Tan, Y.J., Albino, F., 2019. The mechanism of tidal triggering of earthquakes at mid-ocean ridges. Nat. Commun. 10, 2526. https://doi.org/10.1038/s41467-019-10605-2.

Schuster, A., 1897. On lunar and solar periodicities of earthquakes. Proc. R. Soc. Lond. 61, 455–465. https://doi.org/10.1098/rspl.1897.0060.

Senapati, B., Kundu, B., Jha, B., Jin, S., 2024. Gravity-induced seismicity modulation on planetary bodies and their natural satellites. Sci. Rep. 14 (1), 2311. https://doi.org/10.1038/s41598-024-52809-7.

Senapati, B., Kundu, B., Jin, S., 2022. Seismicity modulation by external stress perturbations in plate boundary vs. stable plate interior. Geosci. Front. 13, 101352 https://doi.org/10.1016/j.gsf.2022.101352.

Senapati, B., Kundu, B., Jin, S., Santosh, M., 2024. Drought-induced seismicity modulation in the New Madrid Seismic Zone, central United States. Geosphere. https://doi.org/10.1130/GES02702.1.

Senapati, B., Kundu, B., Perfettini, H., Gahalaut, V.K., Singh, A.K., Ghosh, A., Rao, N.P., 2023a. Fault resonance process and its implications on seismicity modulation on the active fault system. Tectonophysics 861, 229920. https://doi.org/10.1016/j.tecto.2023.229920.

Senapati, B., Panda, D., Kundu, B., 2023b. Solid-Earth Tide Modulations of 2019 Ridgecrest Earthquake Sequence, California: Any Link with Coso Geothermal Field? Journal of Seismology, (Accepted). https://doi.org/10.1007/s10950-023-10166-4.

Shock, E.L., 1992. Chemical environments of submarine hydrothermal systems. Orig. Life Evol. Biosph. 22, 67–107. https://doi.org/10.1007/978-94-011-2741-7_5.

Sibson, R.H., Moore, J.M.M., Rankin, A.H., 1975. Seismic pumping—a hydrothermal fluid transport mechanism. J. Geol. Soc. Lond. 131 (6), 653–659. https://doi.org/10.1144/gsjgs.131.6.0653.

Sohn, R.A., Hildebrand, J.A., Webb, S.C., Fox, C.G., 1995. Hydrothermal seismicity at the megaplume site on the southern Juan de Fuca ridge. Bull. Seismol. Soc. Am. 85 (3), 775–786. https://doi.org/10.1785/BSSA0850030775.

Stroup, D.F., Bohnenstiehl, D.R., Tolstoy, M., Waldhauser, F., Weekly, R.T., 2007. Pulse of the seafloor: tidal triggering of microearthquakes at 9 50′ N East Pacific rise. Geophys. Res. Lett. 34 (15) https://doi.org/10.1029/2007GL030088.

Tan, Y.J., Tolstoy, M., Waldhauser, F., Bohnenstiehl, D.R., 2018. Tidal triggering of microearthquakes over an eruption cycle at 9°50'N East Pacific rise. Geophys. Res. Lett. 45, 1825–1831. https://doi.org/10.1002/2017GL076497.

Tanaka, S., Sato, H., Matsumura, S., Ohtake, M., 2006. Tidal triggering of earthquakes in the subducting Philippine Sea plate beneath the locked zone of the plate interface in the Tokai region, Japan. Tectonophysics 417, 69–80. https://doi.org/10.1016/j.tecto.2005.09.013.

Thomas, A.M., Nadeau, R.M., Bürgmann, R., 2009. Tremor-tide correlations and near-lithostatic pore pressure on the deep San Andreas fault. Nature 462, 1048–1051. https://doi.org/10.1038/nature08654.

Thomas, A.M., Bürgmann, R., Shelly, D.R., Beeler, N.M., Rudolph, M.L., 2012. Tidal triggering of low frequency earthquakes near Parkfield, California: implications for fault mechanics within the brittle-ductile transition. J. Geophys. Res. 117 https://doi.org/10.1029/2011JB009036.

Tolstoy, M., Vernon, F.L., Orcutt, J.A., Wyatt, F.K., 2002. Breathing of the seafloor: tidal correlations of seismicity at axial volcano. Geology 30, 503. https://doi.org/10.1130/0091-7613(2002)030<0503:BOTSTC>2.0.CO;2.

van der Elst, N.J., Delorey, A.A., Shelly, D.R., Johnson, P.A., 2016. Fortnightly modulation of San Andreas tremor and low-frequency earthquakes. Proc. Natl. Acad. Sci. USA 113, 8601–8605. https://doi.org/10.1073/pnas.1524316113.

Vidale, J.E., Agnew, D.C., Johnston, M.J.S., Oppenheimer, D.H., 1998. Absence of earthquake correlation with earth tides: an indication of high preseismic fault stress rate. J. Geophys. Res. 103, 24567–24572. https://doi.org/10.1029/98JB00594.

Warren, N.W., Latham, G.V., 1970. An experimental study of thermally induced microfracturing and its relation to volcanic seismicity. J. Geophys. Res. 75, 4455–4464. https://doi.org/10.1029/JB075i023p04455.

Wessel, P., Luis, J.F., Uieda, L., Scharroo, R., Wobbe, F., Smith, W.H., Tian, D., 2019. The generic mapping tools version 6. Geochem. Geophys. Geosyst. 20, 5556–5564. https://doi.org/10.1029/2019GC008515.

Wiemer, S., McNutt, S.R., 1997. Variations in the frequency-magnitude distribution with depth in two volcanic areas: Mount St. Helens, Washington, and Mt. Spurr, Alaska. Geophys. Res. Lett. 24, 189–192. https://doi.org/10.1029/96GL03779.

Wilcock, W.S.D., 2001. Tidal triggering of microearthquakes on the Juan de Fuca ridge. Geophys. Res. Lett. 28, 3999–4002. https://doi.org/10.1029/2001GL013370.

Wilcock, W.S.D., 2009. Tidal triggering of earthquakes in the Northeast Pacific Ocean. Geophys. J. Int. 179 (2), 1055–1070. https://doi.org/10.1111/j.1365-246X.2009.04319.x.

Wilcock, W.S., Tolstoy, M., Waldhauser, F., Garcia, C., Tan, Y.J., Bohnenstiehl, D.R., Mann, M.E., 2016. Seismic constraints on caldera dynamics from the 2015 axial seamount eruption. Science 354 (6318), 1395–1399. https://doi.org/10.1126/science.aah5563.

Wilson, D.S., 1993. Confidence intervals for motion and deformation of the Juan de Fuca plate. J. Geophys. Res. Solid Earth 98 (B9), 16053–16071. https://doi.org/10.1029/93JB01227.

Zaliapin, Ilya, Ben-Zion, Yehuda, 2013. Earthquake clusters in southern California I: identification and stability. J. Geophys. Res. Solid Earth 118 (6), 2847–2864. https://doi.org/10.1002/jgrb.50179.

Zatman, S., Gordon, R.G., Richards, M.A., 2001. Analytic models for the dynamics of diffuse oceanic plate boundaries. Geophys. J. Int. 145, 145–156. https://doi.org/10.1111/j.1365-246X.2001.00357.x.

Ziv, A., Rubin, A.M., 2000. Static stress transfer and earthquake triggering: no lower threshold in sight? J. Geophys. Res. 105, 13631–13642. https://doi.org/10.1029/2000JB900081.